International Journal of Greenhouse Gas Control 146 (2025) 104428

Contents lists available at ScienceDirect

International Journal of Greenhouse Gas Control

journal homepage: www.elsevier.com/locate/ijggc

Caprock complexity and storage assurance: Advanced findings on CO₂ containment in the Bunter Sandstone Formation

Ali Alsayah [a,b], Sean P. Rigby [a,b,*]

[a] Department of Chemical and Environmental Engineering, Faculty of Engineering, University of Nottingham, University Park, Nottingham, NG7 2RD, UK
[b] Geo-energy Research Centre, University of Nottingham, University Park, Nottingham, NG7 2RD, UK

ARTICLE INFO

Keywords:
Carbon sequestration
Bunter sandstone
Faults
Chimney
Interlayers
Caprock

ABSTRACT

The lower Triassic Bunter Sandstone Formation in the Southern North Sea is a promising site for CO_2 storage. This reservoir has a complex structure, particularly in the overlying Haisborough Group caprock, along with fractured shale interlayers, chimney like-structures and fault features. This study highlighted the importance of incorporating all of this complexity into a model of a 'Bunter-like' storage site.

Given the limited geological data on Bunter, four scenarios (Cases 1–4) were created to assess the impact of CO_2 storage on the integrity of a complex caprock structure. This study revealed that fracture reactivation within variegated shale interlayers differed when comparing scenarios with a multi-layered caprock or a single caprock. With a multi-layered caprock, the CO_2 plume was able to leak via the chimney region, whereas, with a single caprock, it did not. Furthermore, mineral dissolution/precipitation behaviour, particularly halite within the sub-layers of the shale interlayers, varied between the multi-layered and single caprock scenarios. Additionally, greater fault reactivation was observed in multi-layered caprocks compared to single caprock scenarios. With a multi-layered caprock, fault reactivation resulted in increased fault vertical and horizontal permeability than those observed in the single caprock scenario. The presence of a fault traversing several different layers of a multi-layer caprock led to different mineralogical behaviour than with a single caprock.

This study emphasized the critical importance of intricate feedback interactions in systems with complex seal and reservoir geologies, as these interactions are essential for governing the overall behaviour of plume migration.

1. Introduction

The release of carbon dioxide (CO_2) into the atmosphere on a global scale, predominantly driven by fossil fuel combustion, has been a major contributor to global warming and climate change. Geological sequestration of CO_2 has been suggested as a viable strategy to curb the increasing concentration of CO_2 in the atmosphere. As part of the North Sea Transition Deal, the lower Triassic Bunter Sandstone Formation, which is located in the southern North sea, has been established as a priority targeted reservoir interval that may accommodate carbon storage in the UK (Department of Business and Energy and Industrial Strategy, 2022; James et al., 2016).

Structurally, the Bunter Sandstone contains several large periclines (henceforth referred to as Bunter Domes) created by post-depositional halokinesis in the underlying halite-dominated Zechstein Group. The Bunter Sandstone is overlaid by the Haisborough Group which forms a proven seal over several gas fields discovered in the Bunter Sandstone Formation. However, Heinemann et al. (2012) documented spatial variations in the Haisborough Group seal. In the south-eastern portion of the survey area, a thick sequence of chalk overlays the Bunter Sandstone, whereas in the central region, the seal comprises the Solling clay, Röt clay, Röt halite and Muschelkalk layers. Hence, in some regions of the Bunter sandstone, the caprock is complex and multi-layered, whereas in other regions there is a simpler chalk caprock. In previous work we considered the impact on behaviour of an injected scCO2 plume within the underlying reservoir due to differences in the structure and type of caprock (Alsayah and Rigby, 2025). Further, thin shale interlayers have been noted within the reservoir in places (ETI, 2016), and the impact of a simplified model of these has also been considered previously, but in a limited way.

---

* Corresponding author at: [a]Department of Chemical and Environmental Engineering, Faculty of Engineering, University of Nottingham, University Park, Nottingham, NG7 2RD, UK.

E-mail address: sean.rigby@nottingham.ac.uk (S.P. Rigby).

https://doi.org/10.1016/j.ijggc.2025.104428
Received 7 November 2024; Received in revised form 9 May 2025; Accepted 10 June 2025

The structural heterogeneity that is present within the Haisborough Group seal, that is overlaying the Bunter sandstone storage, and within the reservoir itself is much more complex than has been considered before by our group. For example, further heterogeneity is also present in the Bunter Sandstone reservoir within the thin shale interlayers (ETI, 2016). Additionally, the integrity of the Haisborough Group seal that is overlaying the Bunter Sandstone could face challenges due to the presence of faults within the crests of the Bunter domes. These faults are believed to have originated from extensional stresses exerted during the formation of the domes, which occurred concurrently with the movement of the Zechstein Group salts beneath. The presence of faults within the Bunter domes poses a potential hazard to the containment of CO_2. Such faults have the potential to compromise the effectiveness of the caprock seal and may serve as pathways for the migration of CO_2 out of the Bunter Sandstone Formation reservoir into overlying strata. In the most severe scenarios, this could lead to CO_2 migration to the seabed (Gammer et al., 2011).

Further, due to folding processes, fractures may be present in these lithologies, and seismic evidence indicates faulting at the crests of some domes due to extensional stresses during dome formation. These features have the potential to impact storage security, serving as potential migration pathways for CO_2 (Williams et al., 2014; Bentham et al., 2017). The fault system within the Haisborough Group is poorly understood, as there is minimal core data available from this formation (Bentham et al., 2013). There exists a possibility of faults cutting through the Röt formation seal to the Bunter Sandstone. However, data regarding fault characteristics such as cohesion, friction angle, stiffness, etc., are severely limited due to the lack of direct and published information (BP, 2021).

The impact of reservoir heterogeneities, due to geological deposition including interlayers and geological faults, on CO_2 geological storage has been studied. Many sets of workers (e.g. Zhang et al., 2019; Liu et al., 2014; Guo et al., 2016; Kivi et al., 2022; Gao et al., 2023; Zhong et al., 2024) have studied the impact of interlayers on geological CO_2 storage but only using a simplified model with a straightforward arrangement of interlayers. This previous approach utilised an upscaled grid block (a single grid block) to represent the interlayers, and the caprock included in the models was treated as a single impermeable layer. Any effects of caprock heterogeneity on CO_2 behaviour were disregarded, with the analysis focusing solely on the influence of the interlayers. Khudaida and Das (2020) investigated the impact of various interlayer distributions within the reservoir, employing a refined grid to represent these interlayers. However, the model lacks several key parameters, notably the petrophysical heterogeneity within the interlayers, the presence of fractures, and the inclusion of multi-layered caprocks.

Several previous studies (including the ones conducted by Figueiredo et al., 2015; Rinaldi et al., 2014b; Xiao et al., 2020; Liu et al., 2017; Li et al. 2024) have already examined fault stability during CO_2 injection and the potential for leakage, but this analysis was conducted using a simplified 2D model which may result in unrealistic outcomes. However, Alshammari et al. (2022), and Newell and Martinez (2020), investigated CO_2 leakage through faults using a 3D model, but, in these works, the approach used simplified the fault structure by assuming it to be permeable and excluding the possibility of fault reactivation. Further, the studies by Newell and Martinez (2020), Zulqarnain et al. (2020) and Rinaldi et al. (2015) included the caprock solely as a single impermeable layer in their models, while other studies focused on fault analysis and disregarded the presence of the caprock (Romano et al., 2023). In contrast, Rinaldi et al. (2014a) did investigate the behaviour with multi-layered caprocks with faults during CO_2 injection, but only where the model used was a simplified 2D model, which is far from realistic and could lead to misleading results. However, Klimkowski et al. (2015) examined the impact of faults in multi-layered caprocks during CO_2 injection into a producing gas reservoir, for enhanced gas recovery, using a 3D model. Despite incorporating multiple caprock layers, only a single relative permeability curve was applied across all lithologies within the model, and the study disregarded both geochemical interactions and geo-mechanical effects. Hence, earlier studies have generally only used quite simplified models.

Further, previous studies of the CO_2 storage potential of Bunter Sandstone have mainly focused on investigating reservoir capacity and quality, and only paid minimal attention to the long-term implications of potential leakage pathways for CO_2 and/or reservoir brine, and only used a simplified numerical approach that did not include fully coupled Flow-Mechanical-Chemical processes. Such leakage could occur through thin fractured shale and sand sub-layers, and geological faults extending from the reservoir to the multi-layered caprocks over time during CO_2 sequestration (Hollinsworth et al., 2024; Tillero et al., 2024; Aminu and Manovic, 2020; Williams et al., 2013; Agada et al., 2017; Watson et al., 2014; Pekot et al., 2018).

2. Study motivation

This study highlights the importance of accounting for CO_2 plume behaviour in systems characterised by complex geological features relevant to CO_2 storage. A review of previous research reveals a distinct gap in the investigation of such behaviour within formations that include naturally fractured interlayers, geological faults with potential for reactivation, and multi-layered caprocks, whether in the Bunter Sandstone reservoir, or in comparable storage sites worldwide. Building on earlier studies, including our own prior work, this paper examines the leakage risk associated with the introduction of greater geological complexity into the model. In particular, it incorporates a more intricate arrangement of alternating shale and sand sub-layers (‘sandwich-like’ structure) within interlayers located inside the wider reservoir. Furthermore, both heterogeneity and chimney-like features, commonly found in the North Sea, are introduced into the caprock. A geological fault transecting both the caprock and the reservoir is also modelled. These features are included to investigate CO_2 plume behaviour and to enhance understanding of the geochemical and geo-mechanical parameters that influence short- and long-term CO_2 storage and trapping mechanisms in complex geological settings, such as those observed in the Bunter Sandstone reservoir. These additions serve to further complexify our previous models of the Bunter caprock and interlayers, advancing towards a more accurate physical representation. To achieve this, a series of four scenarios was developed using a fully coupled flow–geomechanical–geochemical simulation, applied to a Bunter-like field-scale model, as described in further detail below.

3. Model design

A detailed explanation of the simulator tool and the data used to construct the model is provided in Alsayah and Rigby (2025). This includes the methods used by the CMG-GEM software for simulating processes such as fluid flow, mechanical deformation, and geochemical reactions. The aforementioned data used to build the model, included the injection rate, bottom hole pressure, geological properties, reservoir characteristics, boundary condition, relative permeability, capillary pressure, geo-mechanical properties, and geochemical properties (see supplementary material).

The CMG-GEM simulator was used to create a 3D Cartesian grid structure, specifically developed to model the complex, fully coupled flow-mechanical-geochemical processes associated with injection of greenhouse gases such as CO_2. The model was constructed with a grid of 100 × 10 × 124 (124,000 active grid blocks in total) for Cases 1 and 2, whereas Cases 3 and 4 were constructed with a grid of 100 × 10 × 100 (100,000 active grid blocks in total), but the model dimensions for all Cases 1–4 corresponded to 1054.4 m x 9144 m x 15,240 m.

In light of the limited available knowledge of the Bunter formation itself, this study analyses four distinct abstract cases, each representing different geological structural models for various regions within the Bunter reservoir. Cases 1 and 2 incorporate upper and lower inter-layers (mostly of Bunter Shale) within the reservoir, both comprising 12 sub-layers of Bunter Shale and Sand, each with a thickness of 0.5 m The Bunter shale layers feature natural fractures. Notably, only layers 52 and 81 were susceptible to fracture re-activation, while the remaining Bunter shale inter-layers maintained a fixed fracture permeability of 0.5 mD. Furthermore, Bunter sand layers were interspersed between the shale sub-layers, representing a stack of alternating layers of shale and sand as illustrated in Table 1 and Fig. 1. Further, Cases 3 and 4 represent multi-layered and single caprock-reservoir systems, respectively, but, additionally, including a geological fault into the model. This fault traversed all layers in the K-direction and was exclusively present in layer 5 along the J-direction. Furthermore, it was located 1372 m horizontally from the injection well, as illustrated in Fig. 1. All scenarios are based on a constant injection rate of 0.683 Mt of CO₂ per year over a 50-year period, targeting a total storage of 34.2 Mt of CO₂.

The Barton-Bandis Model (BBM) geo-mechanical approach was utilized to assess alterations, in the fracture permeability of the natural fractures present within the thin shale sub-interlayer, resulting from shifts in effective stress levels (Alsayah and Rigby, 2025). For the fracture properties used in the simulation for Cases 1 and 2, see the supplementary material. Further, a geological fault, as present in the models for Cases 3 and 4, is formed when a portion of the reservoir is dislocated relative to another portion; thence, these dislocated portions are denoted geological fault blocks. Fault blocks extend vertically through the entire reservoir. For convenience, a throw value is applied to the depths of all grid blocks in a fault block. The fluid flow can occur within the fault, and also could flow laterally via the fault from one region to another, and this flow is controlled by the permeability of the fault blocks. If the fault is inactive, the fault block permeability is very small, and fluid cannot flow along or via the fault. In this case, the reactivation will depend on the geomechanically computed stresses on the fault block. The fault reactivation method used in the simulation was as follows. The fault is initially inactive, but once a well induced-pore pressure is applied on it, and overcomes a criterion, the fault is active. Thus, the fault becomes active, and the flow can travel across it and inside it (Kano et al., 2014). The slip tendency is computed using the following definitions, equations and criteria:

$$D_S = \frac{\tau_{max}}{K_t} \tag{Eq.1}$$

If $D_S \geq disp_{critical}$ *then* $slipfric = frcmin$
If $D_S < disp_{critical}$ *then* $slipfric$

$$slipfric = fricoef - \frac{(fricoef - fric\mathrm{min})}{disp_{critical}} D_s \tag{Eq.2}$$

$$ST = \frac{\tau_{max}}{cohes + \sigma'_n * slipfric} \tag{Eq.3}$$

Where:

D_S: Slip displacement.

τ_{max}: Maximum tangential/shear stress on a fault surface = magnitude of sum of vectors τ and s.

K_t: Tangential/shear stiffness coefficient of fault

$disp_{critical}$: Critical displacement

$slipfric$: Mobilized fault friction

$frcmin$: Minimum fault friction

$fricoef$: Friction of fault

σ'_n: Normal effective stress to a fault surface

$cohes$: Fault cohesion

If ST > τ_{max}, the fault will re-activate, and when the fault surface starts moving, fault friction will be decreased. A linear relationship between the fault friction and slip displacement in the hanging wall and foot wall is used.

In the 3D fault plane, three stress components are included: a normal stress (*n*) and two tangential stresses (*t* and *s*) on the fault plane, where the plane passes through the middle points of the fault block (Sanchez and Roehl, 2016).

$$\begin{pmatrix} \sigma'_n \\ \tau \\ S \end{pmatrix} = \begin{bmatrix} n_1 & n_2 & n_3 \\ t_1 & t_2 & t_3 \\ s_1 & s_2 & s_3 \end{bmatrix} \begin{bmatrix} \sigma'_{ii} & \sigma'_{ij} & \sigma'_{ik} \\ \sigma'_{ji} & \sigma'_{jj} & \sigma'_{jk} \\ \sigma'_{ik} & \sigma'_{jk} & \sigma'_{kk} \end{bmatrix} \begin{pmatrix} n_1 \\ n_2 \\ n_3 \end{pmatrix} \tag{Eq.4}$$

n_1, n_2, n_3: Components of unit normal vector n

t_1, t_2, t_3: Components of tangential vector t

s_1, s_2, s_3: Components of tangential vector s

The diagonal shear stress is given by:

$$\tau_{max} = \sqrt{\tau^2 + S^2} \tag{Eq.5}$$

When the slip tendency is less than the maximum slip tendency, the fault is inactive. Thus, the multiplier is then 0. However, if the slip tendency is equal or larger than the maximum slip tendency, then the multiplier will greater than 0 and the fault becomes active. To represent the nature of the faults (sealing or non-sealing), the transmissibility/permeability multipliers are used, which control the cross-fault connection. Transmissibility multipliers are strongly grid dependent and refer to the connection between two grid cells, rather than the fault itself. The multiplier of 0 is used for sealing faults and 1 is for non-sealing faults. The fault properties used in simulation used in Cases 3 and 4 are given in Table 2.

4. Results and discussion

4.1. Cases 1 and 2

This section investigates the CO_2 plume behaviour using two different structures. These are reservoirs with either single or multi-layered caprocks plus a more complex geometry within the reservoir itself involving interlayers made up of stacks of several sand and shale sub-layers (with an overall 'club sandwich-like' disposition).

4.1.1. CO_2 in supercritical phase plume profile

Fig. 2 **(A and B)** shows the $scCO_2$ profile for both Cases 1 and 2 following 50 years of continuous injection. As the injection started, the $scCO_2$ plume migrated upwards towards the lower stack of sand and shale sub-layers under buoyancy forces. Once it reached the first, outer shale sub-layer, it started to spread radially for 613 m in both Cases 1 and 2, since re-activation can only arise for two internal shale bands (sub-layers) within the interior of the interlayer, specifically in layers 52 and 81 in the K-direction within the reservoir, while the rest of the shale sub-layers have a natural fracture with a fixed permeability of 0.5 mD in

Table 1
Shows the set of upper and lower stacked sub-layers of shale and sand in the model for Cases 1 and 2.

Layer number in the K-direction	
Shale	**Sand**
Upper inter-layer section	
46	47
48	49
50	51
52	53
54	55
56	57
58	-
Lower inter-layer section	
75	76
77 and 78	79 and 80
81	82
83	84
85	86
87	-

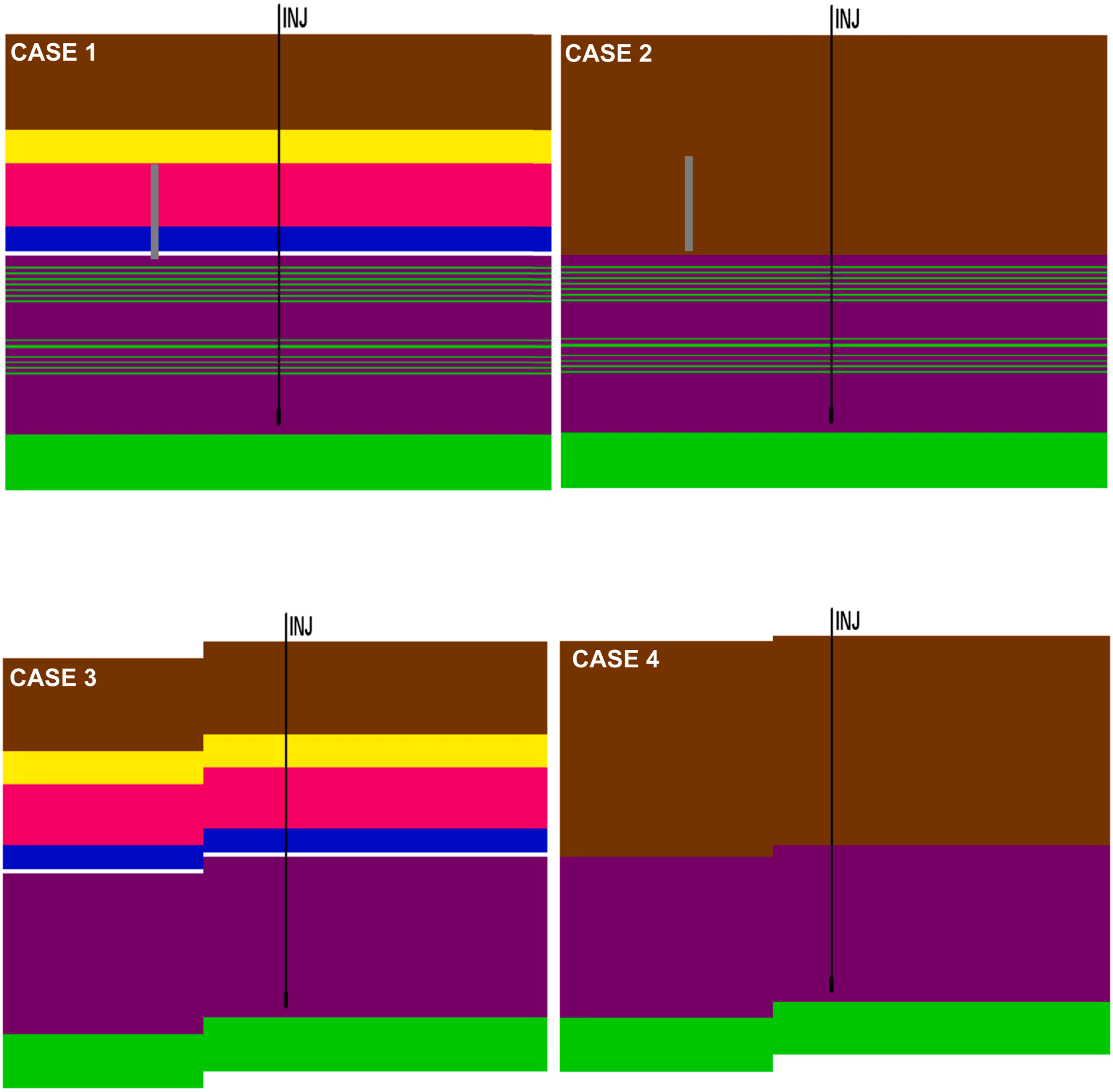

Lithology	Chalk (CH)	Muschelkalk (MCH)	Röt Halite (RH)	Röt Clay (RC)	Solling Clay (SC)	Bunter Sand (BS)	Bunter Shale (BSH)
Thickness (m)	259	91	174	70	3	305	153
Layer number in K direction	1-20	21-25	26-35	36-39	40	41-90	91-100

Fig. 1. Schematic diagrams, presented in an IK cross-sectional view, for all the Cases 1–4 that were utilised in the simulations. In Cases 1 and 2, the thin green layers represent the Bunter Shale inter-layers within the reservoir, while the grey box denotes the chimney structure in the caprock. The colours in the key are those used to distinguish the different lithologies present within the model, along with the corresponding layer thickness and number in the K direction.

both Cases.

As the injection-induced increase in pore pressure accelerated, the pressure propagation reached the lowest shale sub-layer with reactivatable natural fractures, causing further reduction in the effective stress which is normal to the fracture plane. Once this stress reached the threshold value (fracture opening stress), which in this simulation was set to be 7.9 MPa, it caused those fractures within the interlayer located at gridlock 81 in the K-direction to re-activate. Thus, the fracture vertical permeability increased from 1×10^{-8} mD to 233 mD after 5 years of injection in both Cases 1 and 2. This re-activation caused a large vertical

Table 2
Fault properties used in the simulation.

Parameters	Values
Fault throw, m	15.25
Fault friction, dimensionless	0.5
Maximum fault slip tendency, dimensionless	0.001
Fault cohesion, MPa	0.0689476
Fault tangential stiffness, MPa/m	2262
Minimum fault friction, dimensionless	0.4
Critical slip displacement, m	0.0003048

migration of $scCO_2$ via the shale and sand sub-layers. Since the sand sub-layers have the largest permeability compared to the shale sub-layers, thence, a high concentration of the plume accumulated within those sand sub-layers which were partially trapped by the shale layers with natural fractures.

There was a larger build-up of pressure during injection, in the region between the basement Bunter shale and the lower section of the first interlayer within the Bunter sandstone reservoir, exhibited in Case 1, compared to 2. This resulted in, a higher vertical migration, of the plume, from the injection point towards the lower interlayer in Case 1, driven by a more pronounced density contrast between the CO_2 and brine compared to Case 2. Consequently, a larger plume accumulation was impeded by the lower interlayer, leading to a wider lateral spread of

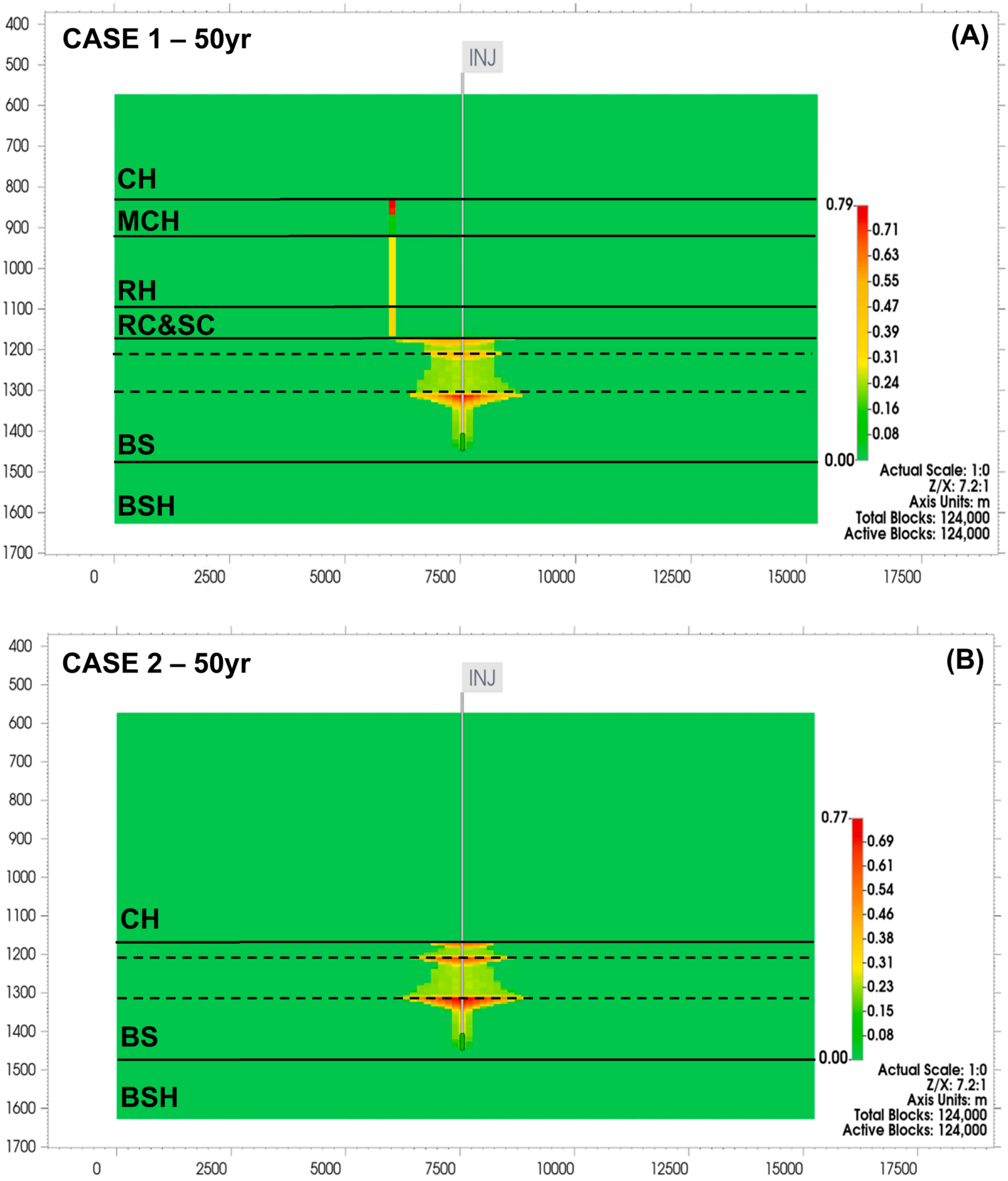

Fig. 2. Spatial distribution of the saturation of supercritical CO_2 (mole fraction) over the simulation period of 50 years, for Cases 1 (A) and 2 (B). The solid lines indicate the location of the boundaries of each lithology in the model.

the plume in Case 1. This in turn, caused a larger area of reactivated fractures in the lower interlayer in Case 1, extending laterally over 5182 m more than in Case 2. After 17 years of injection, the upward migration of the plume was, once more, hindered by the set of shale and sand sublayers in the upper interlayer stack in both Cases as represented in Fig. 2 **(A and B)**.

4.1.2. CO_2 in aqueous phase profile

After 200 years of simulated time, initially, there was an instantaneous increase in the fraction of dissolved CO_2 since the injected supercritical CO_2 comes into direct contact with the native brine, but, as a local equilibrium becomes established between the supercritical CO_2 ($scCO_2$) and brine, the rate of CO_2 dissolution cannot keep up with the injection rate, and the mole fraction of $scCO_2$ rises rapidly. However, during the post-injection period, a reduction in the $scCO_2$ plume was observed as more CO_2 goes into solution due to the relative permeability hysteresis and capillary forces. The dissolved CO_2 plume further expanded vertically and laterally, but despite this plume expansion, the plume in Case 2 did not enter the chimney as seen in Fig. 3 **(A and B)**. This particular situation arose because of the more restricted lateral expansion of the $scCO_2$. Thus, less dissolved CO_2 was available to migrate horizontally. Later in the simulation time (1000 years), convective fingering can be observed in both Cases (caused by density instability). Moreover, in Case 1, the plume expanded more substantially within the caprock region covering a larger region, by 206 m vertically and 1371 m horizontally, compared to Case 2, including all of the Solling Clay, Röt Clay, Röt Halite, and Muschelkalk as represented in Fig. 3**(C and D)**. The fingering observed in Fig. 3**(A–D)** is driven by two thin Bunter Shale layers that initially retained CO_2 but fractured during injection. Reflecting realistic subsurface behaviour, the Barton-Bandis model indicates that fractures, once reactivated, do not fully close. This partial opening, combined with gravitational instability and heterogeneous fracture permeability, enabled downward fingering of CO_2-rich brine and enhanced convective flow.

4.1.3. Geo-mechanical

Fig. 4 illustrates the BHP profiles for Cases 1 and 2 over time. Initially, Case 1 exhibits a higher pressure than Case 2. This discrepancy is attributed to the differing re-activation periods of fractures within the interlayers and the presence of leakage via the chimney in Case 1, which did not occur in Case 2. Consequently, the pressure profiles between the two cases diverge, leading to variations in mean effective stress and vertical displacement, as depicted in the Figs. 5 **(A and B) and** 6**(A and B)**. Notably, in the Bunter sandstone reservoir, Case 2 displays a smoother change in mean effective stress and vertical displacement compared to Case 1. As seen in Fig. 5**(A and B)**, sudden changes in effective mean stress, especially within the Bunter Sandstone reservoir, are primarily driven by the presence of multiple thin, fractured shale interlayers. Fracture reactivation within these layers directly influences the reservoir pressure profile, which is inversely related to effective stress.

The pore pressure profile of the reservoir region between the lower and upper inter-layer stacks of shale and sand sub-layers was different between Cases 1 and 2. A larger pressure build-up in this region was observed in Case 1 compared to Case 2 in the year 2039 as shown in Fig. 7, not only before the re-activation of the upper interlayer, but the larger increase in pore pressure continued even after the occurrence of the upper interlayer re-activation. This was due to all of the natural fractures in the lower interlayer being re-activated from 1×10^{-8} mD to 233 mD in Case 1. In contrast, in Case 2, fracture re-activation resulted in a permeability increase from 1×10^{-8} mD to 35 mD, and this change occurred far from the injection zone as illustrated in the Fig. 9**(A and B)**. Therefore, in Case 1, this allowed more brine to leak via the lower interlayer towards the upper interlayer causing a larger build-up of pore pressure in the zone between the lower and upper interlayer stacks, when compared to Case 2.

This, in turn, led to a larger increase in pressure within the upper interlayer fractures by 0.3 MPa in Case 1, compared to Case 2, in the year of 2041, resulting in larger reduction in effective normal stress to the fracture plane, and a faster approach to the fracture opening stress threshold. Therefore, the fracture re-activation within the upper interlayer occurred one year earlier in Case 1, compared to Case 2, as displayed in Figs. 8–11. As consequence, in Case 1, the $scCO_2$ plume reached the Solling Clay caprock basement 2 years earlier, and with higher $scCO_2$ concentration by 19 %, compared to the arrival of the plume at the bottom of the caprock in Case 2.

In addition, the fracture within the upper interlayer in Case 2, reactivated by shear slip, but, at a later stage of injection (year 2069), exhibited tensile failure as the normal fracture effective stress became below zero. In contrast, in Case 1, the upper interlayer fracture only reactivated by shear slip as illustrated in Fig. 11.

The earlier fracture re-activation within the upper interlayer, that occurred in Case 1, contributed towards the pressure rise in the region between the chimney and upper interlayer by allowing brine and $scCO_2$ to escape via the fracture towards this zone. After 50 years of injection, the $scCO_2$ plume shape for both Cases was not symmetric. As the plume reached the caprock basement, the presence of the chimney within the caprock in both Cases came into play in terms of controlling the plume lateral migration where a larger pore pressure difference, between the injection zone and under the chimney region, of 0.43 MPa was observed in Case 1 compared to the lower value of only 0.06 MPa for the corresponding difference in Case 2, as seen in Fig. 12. Thus, the plume lateral migration was faster towards the chimney, under the advection force, in Case 1 compared to Case 2.

4.1.4. Geochemical processes

In Cases 1 and 2, the CO_2 total concentration in the aqueous phase increased sharply, indicating the quick establishment of equilibrium between the aqueous and gas phases. Correspondingly, the pH decreased sharply as CO_2 dissolved in both Cases. After 1000 years of simulation time, the pH in the reservoir reduced from 7.1 to 5.2 in Case 1 and to 5.4 in Case 2. This drop in the pH was mainly controlled by the presence of $scCO_2$ in the short term, but, in the long term, brine convection and mixing controlled the pH drop in regions without $scCO_2$ (André et al., 2007). Further, the zone of the lowered pH extended about 403 m vertically and 5334 m laterally in Case 1 while, only, 72 m vertically and 2896 m horizontally in Case 2. Therefore, after 1000 years of simulation time, the spatial-temporal evolution of the CO_2 plume roughly followed the gas saturation pattern. Also, a noticeable instability in the pH was seen within the chimney in Case 1. Namely, the pH value increased from 5.4 to 5.9 in the year 2240 as illustrated in Fig. 13**(A and B)**. This was caused by the higher CO_2 fugacity increases due to the amount of dissolved CO_2 in the native brine. Further, there was greater calcite dissolution within the chimney in Case 1 compared to Case 2. This resulted in a reduction in the hydrogen ions in the aqueous phase, due to the calcite reaction with acids, namely, carbonic acid (derived from CO_2 dissolution). This reaction consumes H^+ ions, thereby increasing the pH of the solution. In contrast, no rise in pH was seen in Case 2 due to the lack of a $scCO_2$ presence in the chimney as shown in Fig. 14.

Additionally, the presence of stacked thin shale and sand sub-layers within the upper and lower sections of the Bunter Sandstone reservoir caused the minerals to behave differently from seen with more simplified models. For example, after a simulated period of 1000 years, halite precipitation was the dominant change within the upper and lower stacked interlayers in Case 1, while halite dissolution was the primary change in Case 2 as represented in Fig. 15**(A and B)**. This was due to the varying amounts of $scCO_2$ plume accommodated in these layers to dissolve in the resident brine, which was controlled by the reactivation of the interlayer fractures. These findings contrasted with the results obtained by Alsayah and Rigby (2025), who included two continuous (unlayered) shale inter-layers, as shown in Fig. 15 (C and D, but with reservoir models otherwise akin to Cases 1 and 2. It is evident that the

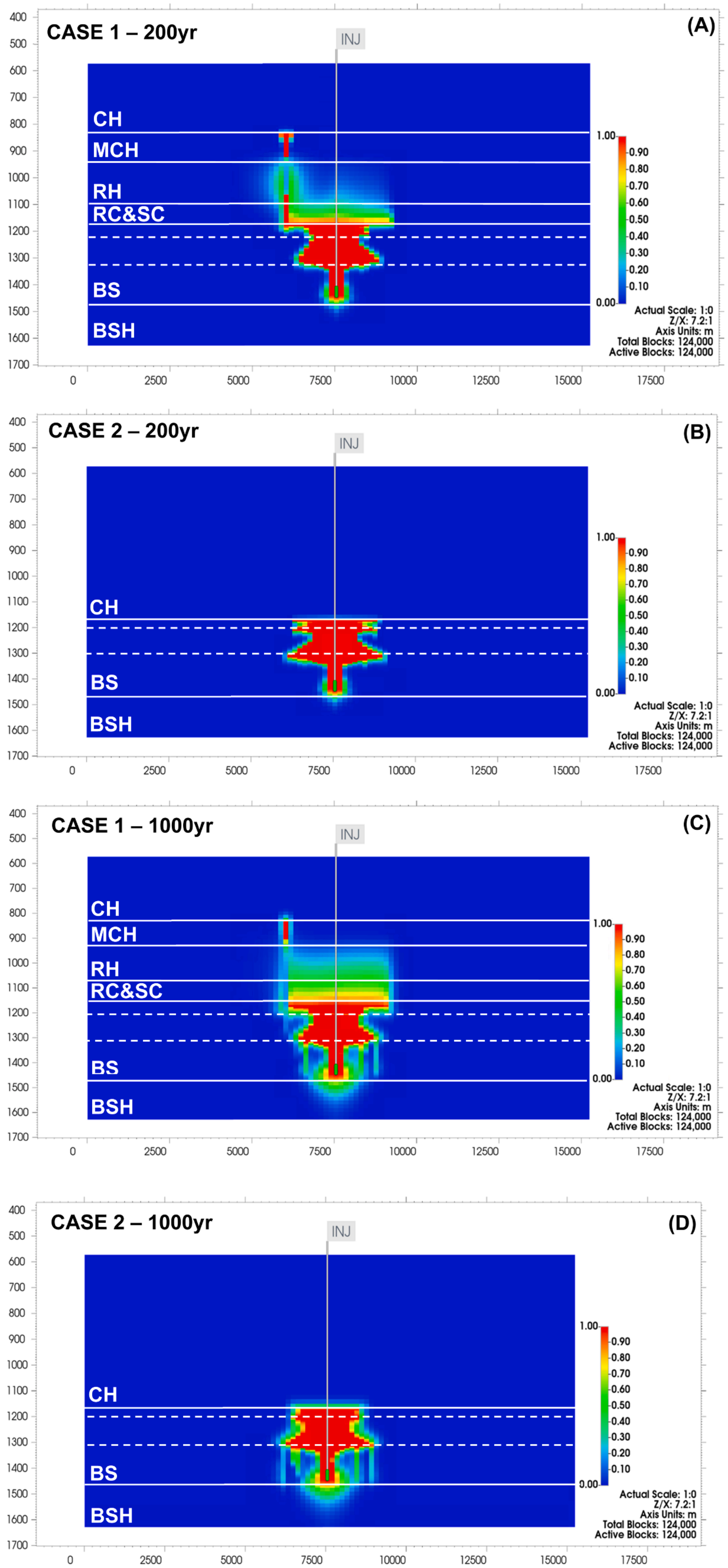

Fig. 3. Spatial distribution of the dissolved CO_2 mole fraction over the injection-period for Cases 1 and 2 (A&B) for 200 years simulation period, Cases 1 and 2 (C&D) shows 1000 years of simulation period, respectively. The solid lines indicate the locations of boundaries of each lithology, and the dashed lines represent the inter-layer locations in the model, respectively.

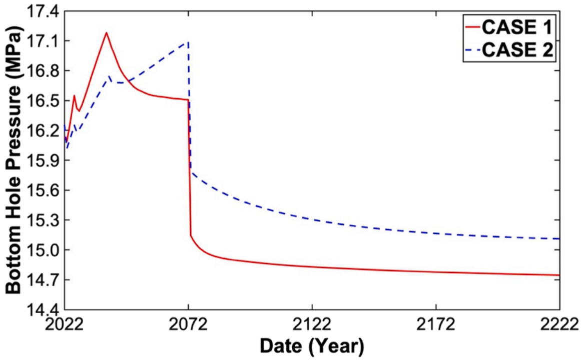

Fig. 4. BHP change as a function of time for both Cases 1 and 2.

new Cases 1 and 2 demonstrated clear heterogeneity in halite change (precipitation and dissolution) within both interlayers. Thus, the inclusion of a detailed and complex set of interlayers within the reservoir would lead to noticeable and important differences in mineral behaviour within these interlayers that affect permeability.

Since the simulation period was only 1000 years, the time was limited for most of the minerals to exhibit a dramatic change, except for calcite. Thus, the change to calcite was the primary mineralogical variation that controlled the porosity change of the different caprocks in both Cases 1 and 2. The caprocks in Case 1 showed more geochemical activity than in Case 2. This is because of the CO_2 leakage from the reservoir towards the caprocks via the chimney causing acidification of the native brine, which is favourable for the calcite dissolution and precipitation within the caprocks in both Cases 1 and 2. Moreover, halite instability was observed in Case 1 resulting from the multi-layered nature of the caprocks compared to a single caprock wherein the halite is much more stable as shown in Fig. 16. The change in the halite was influenced by the abundance of HCO_3^-, since a high concentration of HCO_3^- reduces the precipitation of halite in the presence of CO_2.

The caprocks underwent changes in porosity as seen in Fig. 17**(A and B)**. Comparing the caprock porosity change in both Cases 1 and 2, it can be observed that the porosity change arose from the change in mineral volume fraction. In Case 1, the Röt Halite caprock layer exhibited a noticeable increase in porosity, relative to the other caprock layers, by 0.3 % during the 2230 years of simulation time, and this rise was caused by the calcite dissolution. However, from year 2231 to 3032, a reduction in porosity by 0.1 % was observed due to calcite precipitation as illustrated in Fig. 17 **(A and B)**. In contrast, in Case 2, the Chalk caprock porosity rose by 0.1 % which was a result of calcite dissolution. It should be noted that any change in caprock porosity directly influences permeability, but, in both Cases considered here, the variation in porosity is too minor to result in a large change in permeability.

Comparing the results from the previous study (Alsayah and Rigby, 2025), which focused on the scenario with two thick, continuous shale-only inter-layers, to those of the complex thin shale and sand sub-layers used in this work, it is evident that the overall CO_2 plume behaviour differs noticeably. In the case of stacked thin shale sub-layers, vertical migration of the plume was restricted, causing a wider lateral

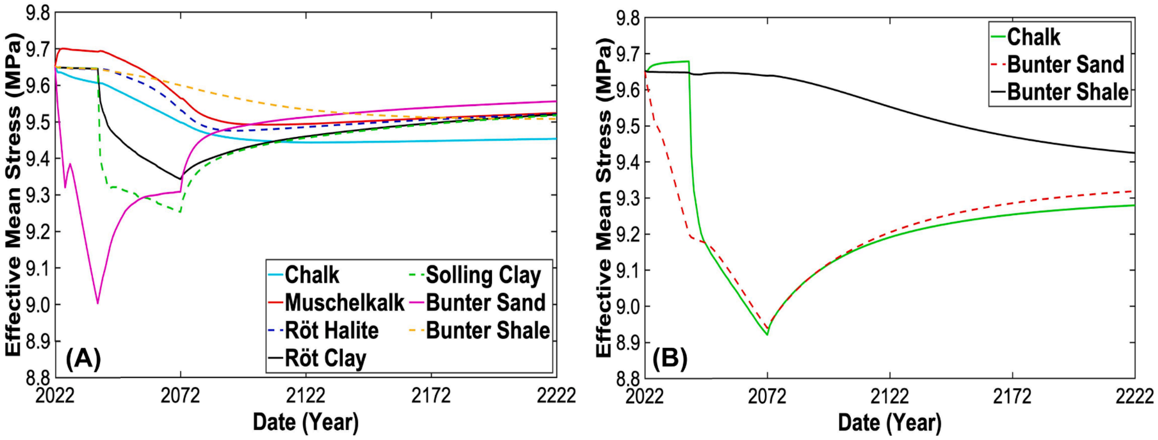

Fig. 5. Effective mean stress of each lithology within the model for Cases 1 and 2 after 200 years of simulation, with parts A and B corresponding to Cases 1 and 2, respectively.

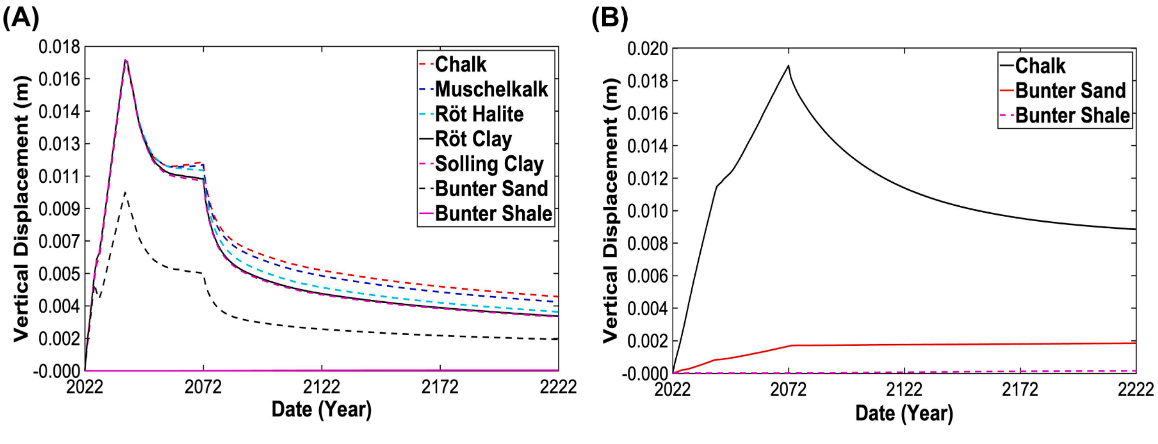

Fig. 6. Volumetric expansion (ground uplift) of the reservoir and caprocks during the 200 years of simulation for Cases 1 (A) and 2 (B).

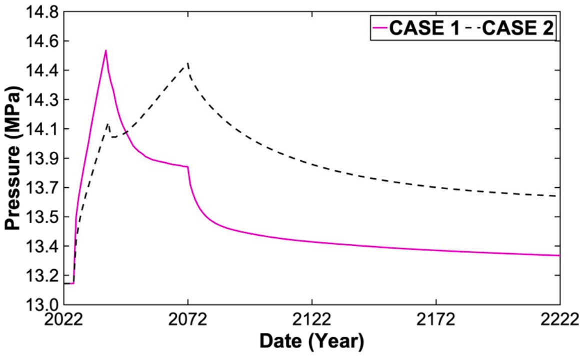

Fig. 7. The pressure in the Bunter Sandstone region, positioned between the upper and lower (interlayer) stacks of shale and sandstone, as a function of time for both Case 1 and Case 2.

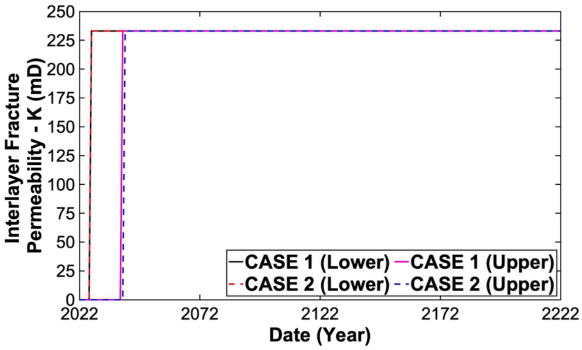

Fig. 8. Changes in fracture permeability of the upper and lower interlayers over time near the injection zone for both Case 1 and Case 2.

spread within the thin sand sub-layers. This resulted in a greater amount of CO_2 being trapped within the thin sand sub-layers, compared to the two thick shale-only inter-layers scenario.

In the two thick shale inter-layer scenario, fractures within the shale layers reactivated earlier, failing to effectively contain the vertical migration of the CO_2 plume. In contrast, for the thin shale sub-layers (as seen in Cases 1 and 2), fracture reactivation occurred later in the simulation. This delay was due to the presence of thin shale sub-layers with a fixed fracture permeability of 0.5 mD, combined with sand sub-layers that had high horizontal permeability. These factors limited the ability of the plume to reach the upper thin shale sub-layer that has a fracture reactivation option. As a result, less of the plume accumulated beneath the upper thin shale layers, leading to a smaller increase in pore pressure (less reduction in normal fracture effective stress) during the injection period, which delayed the fracture reactivation.

A notable difference emerged in the overall CO_2 trapping mechanisms after 1000 years of simulation. Compared to the two thick shale inter-layers scenario from the earlier study (Alsayah and Rigby, 2025), the sandwich-like structure scenarios (Cases 1 and 2) demonstrated a higher percentage of CO_2 trapped by hysteresis, with an increase of approximately 6 %.

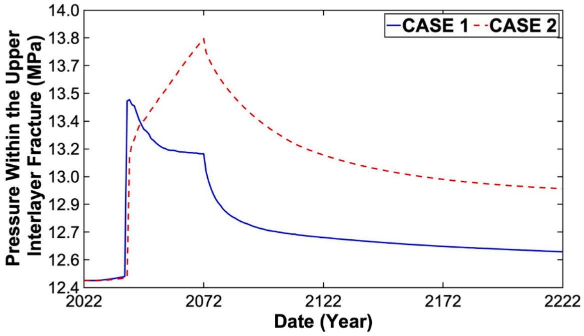

Fig. 10. The pressure within the fracture of the upper interlayer overtime in both Cases 1 and 2.

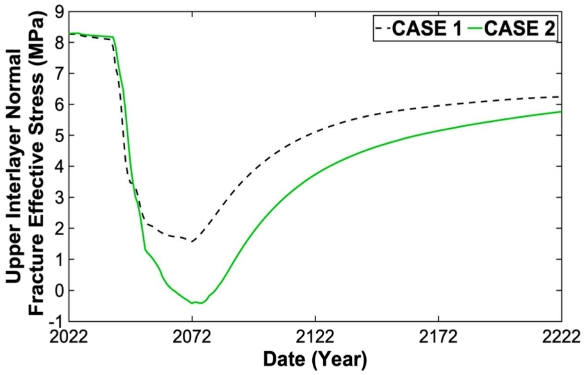

Fig. 11. Effective normal fracture stress of the upper interlayer overtime of both Cases 1 and 2.

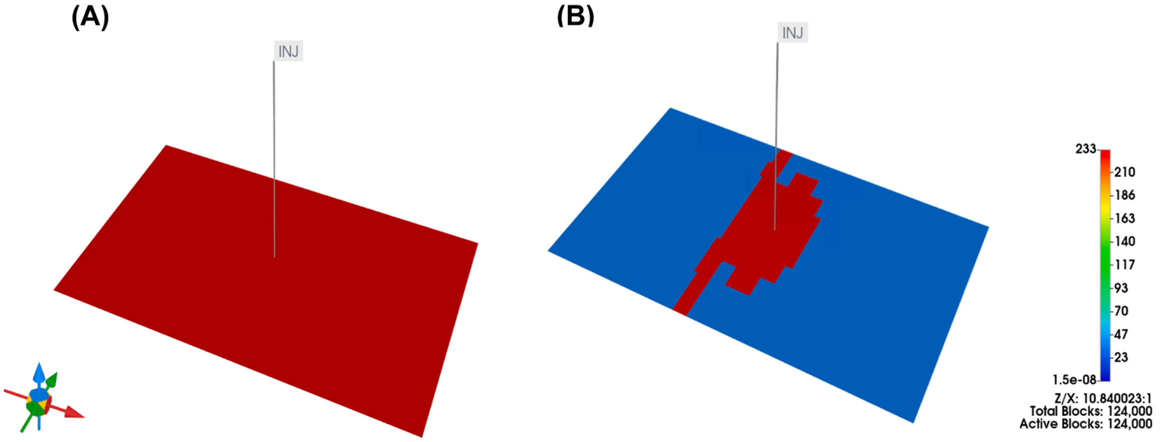

Fig. 9. 3D maps of the upper interlayer vertical permeability for both Cases 1 and 2, denoted as (A) and (B) respectively after 50 years of injection. The scale indicates the vertical permeability in millidarcies (mD).

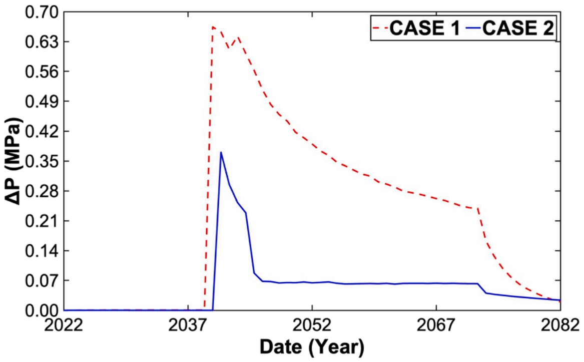

Fig. 12. The pressure difference between the near injection zone and the area under the chimney zone for both Cases 1 and 2.

4.2. Cases 3 and 4

Cases 3 and 4 show the importance of detailed modelling of the internal structure of caprocks and their impact on the fault re-activation when computing fully coupled mechanical-chemical reservoir numerical simulations to assess the CO_2 plume migration.

4.2.1. Profile of the supercritical phase CO_2 plume

Fig. 18**(A and B)** indicate the spatial distribution of $scCO_2$ saturation after 50 years of injection in terms of mole fractions. After 50 years of injection, in Case 3, once the $scCO_2$ plume reached the Solling Clay caprock, it started to migrate laterally by 3657 m, whereas, in Case 4, the plume expanded laterally, once it reached the Chalk caprock, by 3803 m. The location of the fault is 1371 m laterally away from the injection well, and where the initial state of the fault is assumed to be sealed in both Cases 3 and 4. The lower lateral spread of the plume observed in Case 3 was due to the plume leakage via the re-activated fault. Further, the $scCO_2$ managed to migrate upwards via the fault by 280 m, thereby

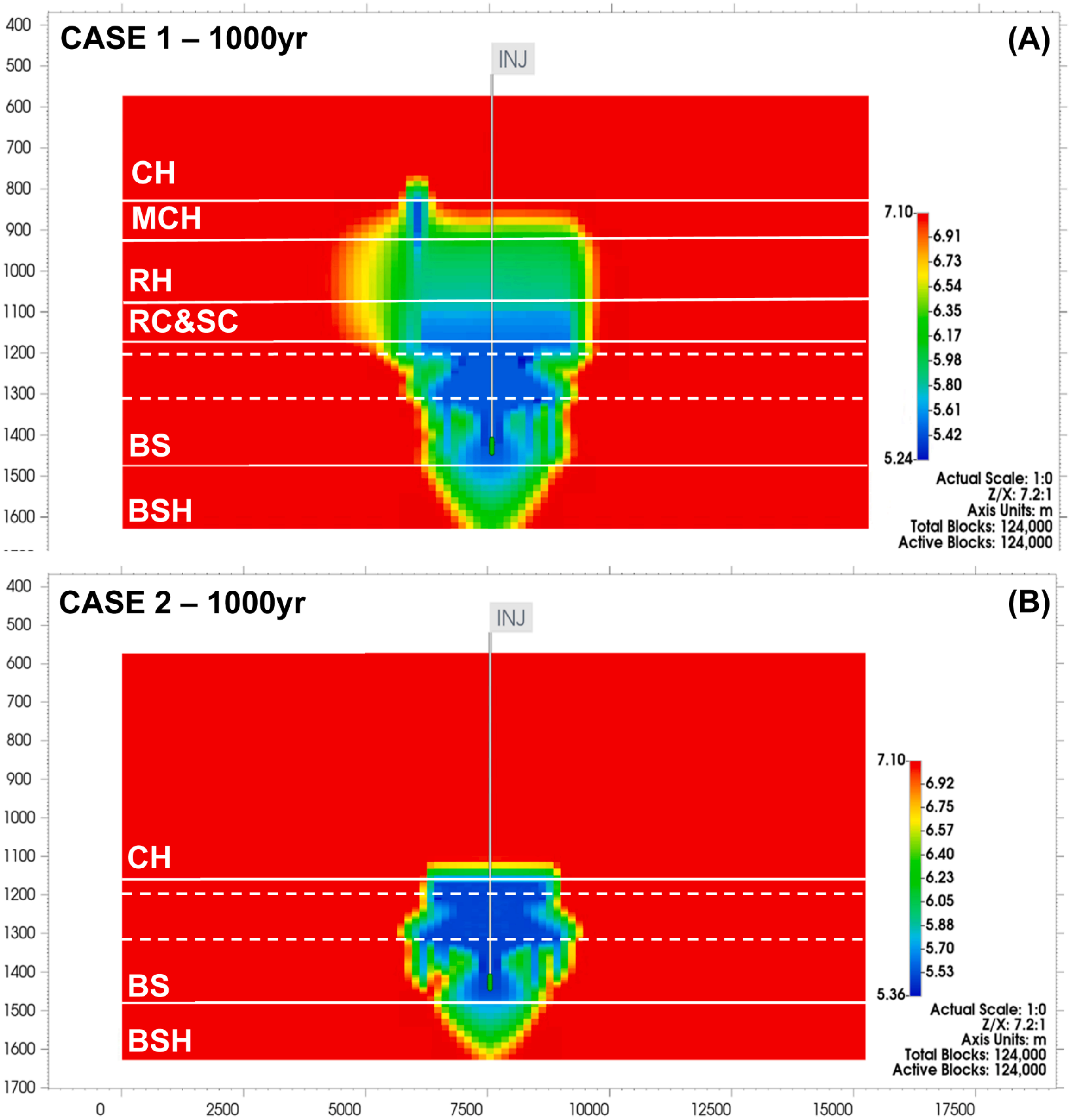

Fig. 13. The pH profile after 1000 years of simulation time for both Cases 1 (A) and 2 (B) is shown. The solid white lines indicate the boundaries of lithologies in the model, while the dashed lines represent the interlayers within the reservoir. The scale displays the pH values.

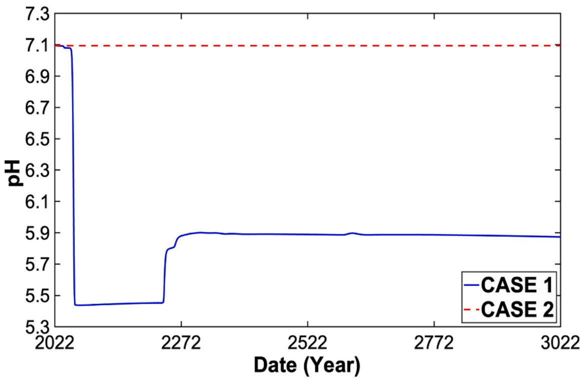

Fig. 14. pH change within the chimney as a function of time for both Cases 1 and 2.

reaching the basement of the Muchelkalk caprock. Whereas, in Case 4, the plume only leaked along the fault by 20 m causing uneven migration of the CO_2 plume.

From the simulation results it can be concluded that the fault stability in Case 4 is weaker compared to Case 3. While the fault was re-activated after just 1 year of injection in Case 4, in contrast, in Case 3, it was re-activated only after 25 years of injection. During injection, brine is moved by the CO_2 plume towards the fault. Pressure propagates before mass transport of $scCO_2$, so, in other words, the pressure front travels ahead of the $scCO_2$ plume, resulting in the fault re-activating earlier than the arrival of $scCO_2$, creating hydraulic communication between the storage reservoir and saline formation. The hydraulic connection allows for pressure to be relieved from the storage formation and allows for the re-establishment of hydraulic equilibrium. The plume does not encounter the fault itself until after 25, or 28, years of injection in Cases 3 and 4, respectively.

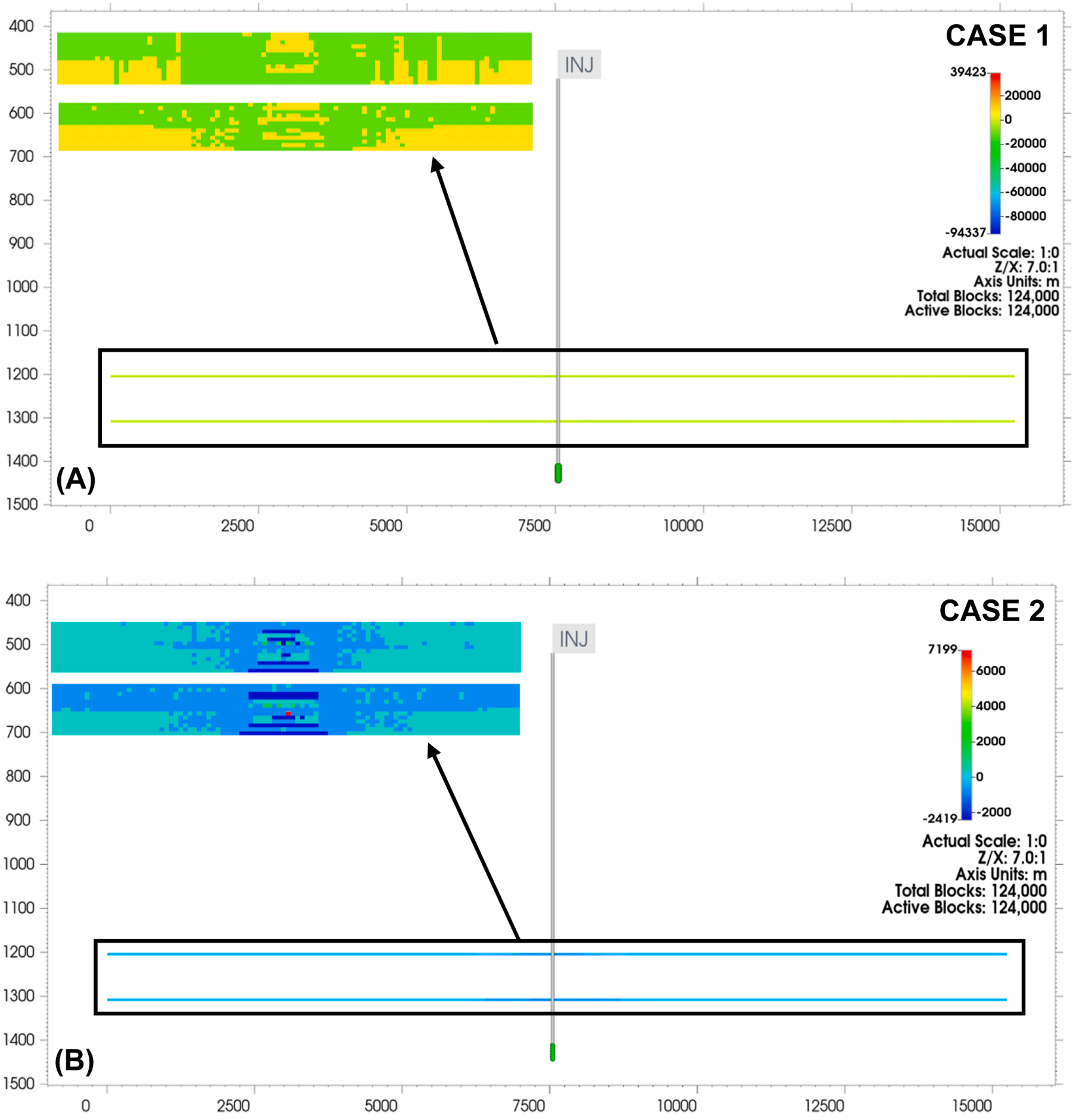

Fig. 15. 2D view depicting the change in halite concentration within the upper and lower stacked sand and shale interlayers after 1000 years of simulation for Cases 1 (A) and 2 (B), and also for two thick, continuous interlayers in the single caprock system (C) and multi-caprocks system (D) (Alsayah and Rigby, 2025). A magnified inset in the top left corner highlights both interlayers, and the stacked sub-layers of sand and shale, indicated by a rectangular box. The scale displays the change in halite concentration (kgmole), and the ruler shows the length in metres.

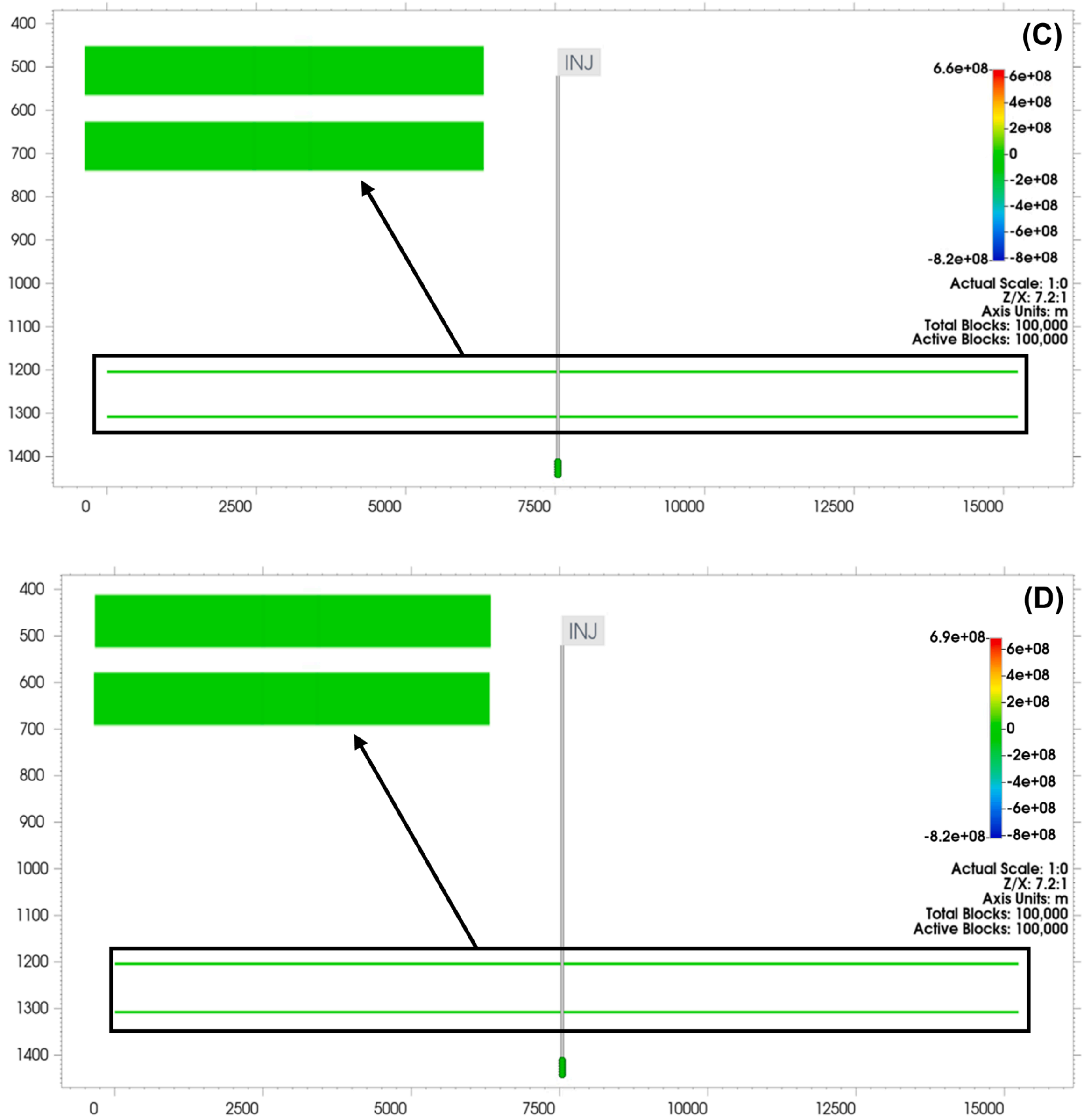

Fig. 15. (*continued*).

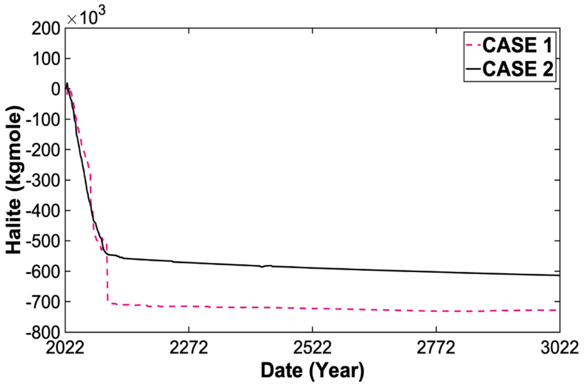

Fig. 16. Variation in Halite as a function of time at field scale for both Cases 1 and 2.

4.2.2. Profile of the CO_2 in the aqueous phase

Fig. 19**(A–D)** show the spatial distribution of the mole fraction of dissolved CO_2 at temporal intervals of 200 and 1000 years. After 200 years of simulation, the dissolved CO_2 plume in Case 3 migrated further into the caprocks, including, the Solling clay, the Röt Clay, Röt Halite, Muschelkalk, and lower section of the Chalk layer, via a diffusive transport mechanism. Also, lateral migration, from the fault, to both sides within the caprocks was observed due to the increase in the fault horizontal permeability during the re-activation period. In contrast, the plume migration into the Chalk caprock was limited in Case 4 because of the lack of $scCO_2$ present in the caprock to dissolve in the resident brine. Furthermore, at the end of simulation (1000 years), the plume coverage across the caprock region was larger in Case 3 compared to Case 4 by 222 m vertically and 608 m horizontally.

4.2.3. Geo-mechanical processes

Fig. 20 illustrates the change in BHP over time for both Cases 3 and 4. Comparing both Cases, the BHP profile maximum was noticeably larger in Case 4 compared to Case 3 by 0.2 MPa. Due to less fault re-activation in Case 4, a larger BHP was observed compared to Case 3 before the end

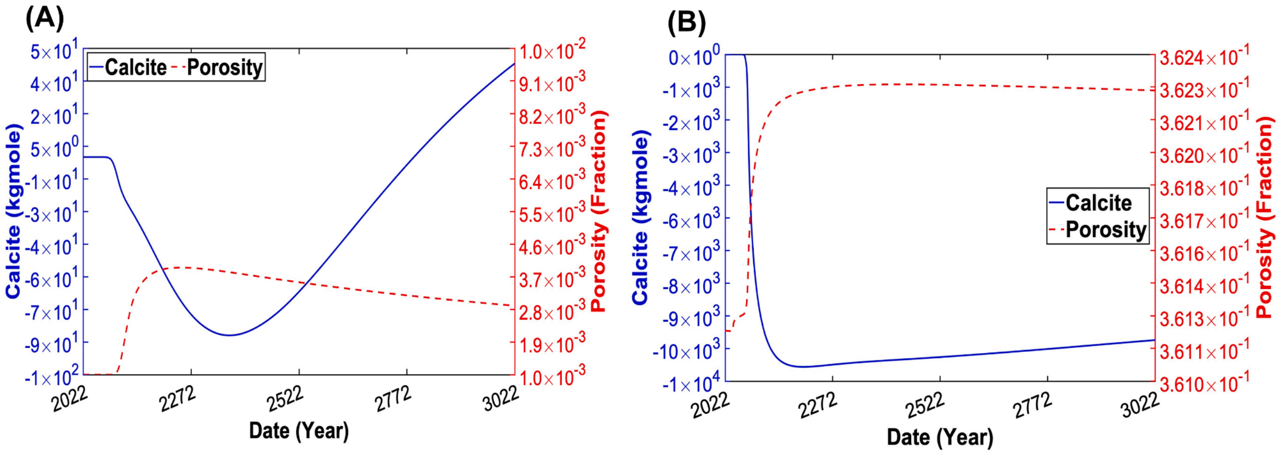

Fig. 17. Curves showing calcite variation (kgmole) and porosity change over time for a particular caprock in each of Cases 1 and 2. In Case 1, it is Röt Halite (A). In Case 2, it is the Chalk (B). Positive values in the data indicate precipitation, whereas negative values indicate dissolution.

of injection. Further, the BHP fell after injection was concluded, to approximately 14.8 MPa and 15.1 MPa in Cases 3 and 4, respectively. Consequently, both Cases experienced a reduction in effective mean stress and an increase in vertical displacement. Notably, the Chalk caprock uplift was larger by 0.01 m in Case 3 compared to Case 4. This difference is attributed to the lower increase in the fault permeability due to re-activation in Case 4, which further increased pore pressure and reduced mean effective stress within Chalk caprock, as shown in the Figs. 20–22.

The reservoir stress path describes the degree to which the minimum horizontal stress changes in response to perturbations of pore fluid pressure during injection (Vilarrasa et al., 2010). The pore pressure and effective stress disturbances are strongly altered by the parameters of the fault zone. The main factors that influenced the stability of the fault in both cases are the rock mechanical properties and heterogeneities of the caprocks. The fault stability and stress states were assessed based on the evaluation of the ratio of shear stress to effective normal stress, known as slip tendency analysis, which is expressed by the Mohr-Coulomb criterion. As the injection started, the increase in pore pressure led to a decrease in the effective normal stress on the fault surface in the lower section of the fault in Cases 3 and 4, as seen in Fig. 23. During the early stages of injection, this reduction in effective normal stress was larger, in Case 3 compared to Case 4, by 0.002 MPa. The pressure induced by the injection process triggered the expansion of the reservoir (poro-elastic effects), resulting in increased stresses due to the pressure exerted by this expansion. Consequently, there were alterations in shear stress within the fault zone. This phenomenon originated from the reduction in effective normal stress on the fault plane, as per Terzaghi's principle, leading to a decrease in fault shear strength. This effect was particularly pronounced at the interface between the fault zone and the caprock, especially in the lower section of the fault (Mazzoldi et al., 2012; Clayton et al., 1995). Thus, the slip strength weakens and the slip tendency increases as long as the least principal compressive stress is constant (Morris et al., 1996). As a result, the slip tendency profile that was observed in Cases 3 and 4 was different as shown in Fig. 24.

Since the maximum fault slip tendency was chosen for both Cases to be 0.001, the fault will re-activate once the slip tendency reaches this value. It can be observed that a longer time was required for the multi-layered caprock system (Case 3) to reach the value of 0.001 compared to Case 4 which caused the delay in fault re-activation in Case 3 as seen in Fig. 24. The CO_2 plume extends laterally far from the injection point in both Cases 3 and 4 under the advection transport mechanism. Despite this, the plume reached the fault zone simultaneously in both cases. In Case 3, fault reactivation resulted in a significant increase in both vertical and horizontal permeability. Specifically, the fault's vertical permeability in the Solling Clay caprock increased from 0.17 mD to 13.3 mD, and within the Röt Clay and Halite caprocks, it increased from 0.01 mD to 0.67 mD, as shown in the figure. Conversely, in Case 4, the vertical permeability within the Chalk caprock increased from 0.01 mD to 0.67 mD as illustrated in Fig. 25**(A and B)**.

Additionally, the horizontal permeability within the fault zone in Case 3 increased from 1.1 mD to 72.5 mD in the Solling Clay. In contrast, in Case 4, the horizontal permeability of the Chalk within the fault zone increased only from 0.1 mD to 6.2 mD, as shown in the Fig. 26. Therefore, the vertical and lateral migration of the plume within the fault was greater in Case 3 compared to Case 4, contributing to a larger CO_2 plume leakage via the fault. Consequently, the pressure build-up length along the fault was also enlarged. The extent of fault reactivation is influenced by the in-situ stress anisotropy and the reservoir's permeability. Also, due to the barrier effect of the fault, which was caused by the late fault re-activation in Case 3 compared to Case 4, the build-up of pore pressure within the fault is higher than that in the bulk reservoir.

The characteristics of pressure build-up and brine migration are strongly affected by the properties of the overlying and underlying confining units (Cavanagh and Wildgust, 2011). The pressure perturbation from CO_2 injection caused considerable transfer of brine from the reservoir vertically upwards towards the caprock. At the early stage of injection, the CO_2 displaces the native brine in the area very close to the injection zone, and the strong build-up in pressure was caused by the larger driving forces required to move the resident brine away from the injection zone (Pruess and Garcia, 2002). During the post-injection period, the pressure does not return to its initial value, and, hence, the stresses are different within the damaged zone. The vertical permeability of the damaged zone within the fault changes in response to the reduction in pressure caused by the shut-in of the injection well. This reduction in pressure leads to an increase in the normal effective stress to the fault plane which is a combination of the in-situ stresses applied perpendicular to the fault surface, causing the slip tendency to become smaller than the set value for the maximum slip tendency. Thus, the fault permeability faced a reduction from 0.63 mD to 0.1 mD in Case 4 as shown in the Fig. 25**(A and B)**. In contrast, in Case 3, the fault permeability is kept constant at its maximum value due to the slip tendency still being larger than the maximum slip tendency.

4.2.4. *Geochemical processes*

Since the value of pH is related to the amount of dissolved CO_2 in the native brine, then the pH following the injection of $scCO_2$ into the reservoir reduced by 1.8 in Case 3, and by 1.9 in Case 4, by the end of simulation. This moderate change confirms that the carbonic acid formed is a weak acid. Further, the larger pH value that was observed, in

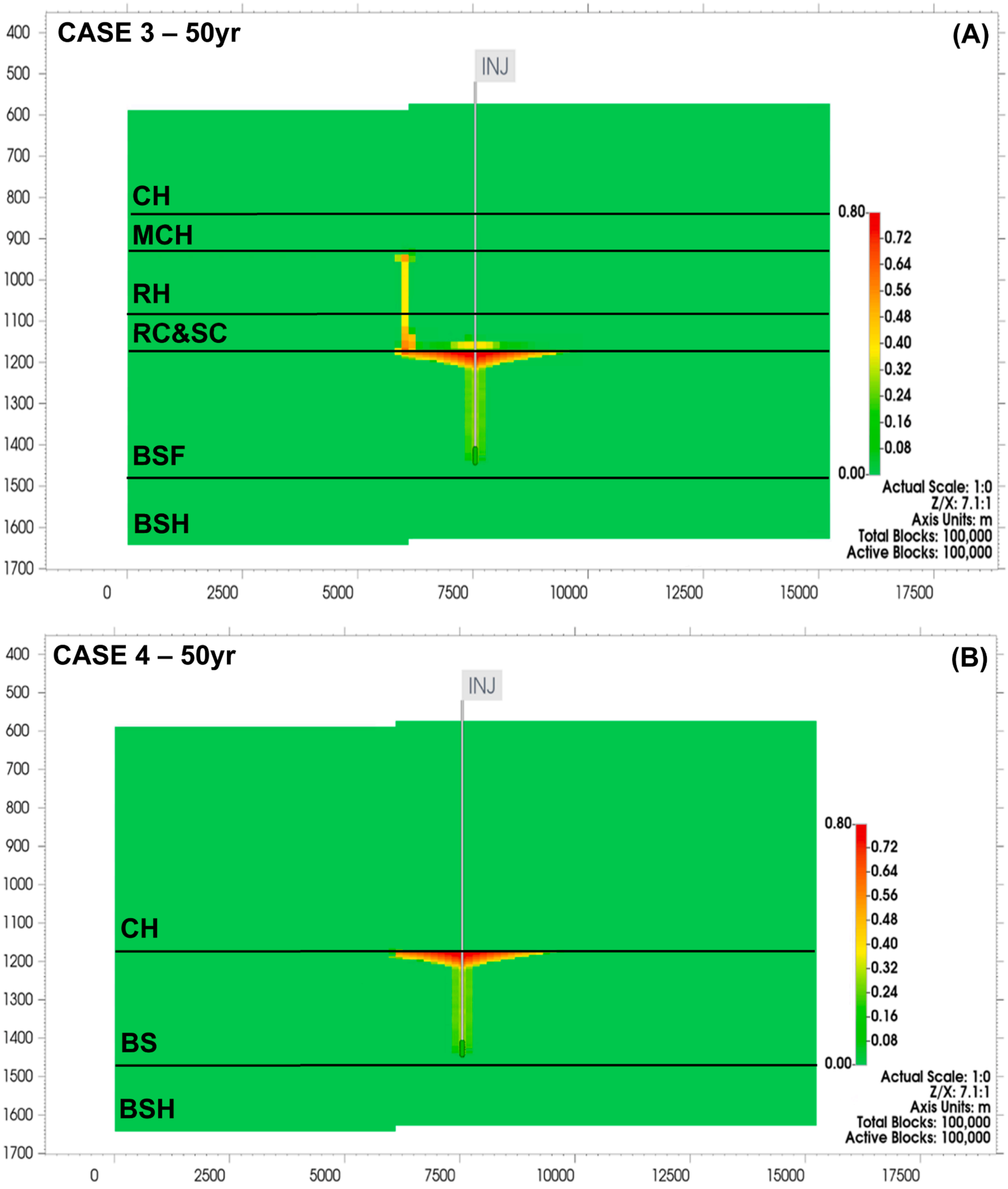

Fig. 18. Spatial distribution of the saturation of supercritical CO_2 (mole fraction) over injection period of 50 years, for Cases 3 (A) and 4 (B). The solid lines indicate the location of the boundaries of each lithology in the model.

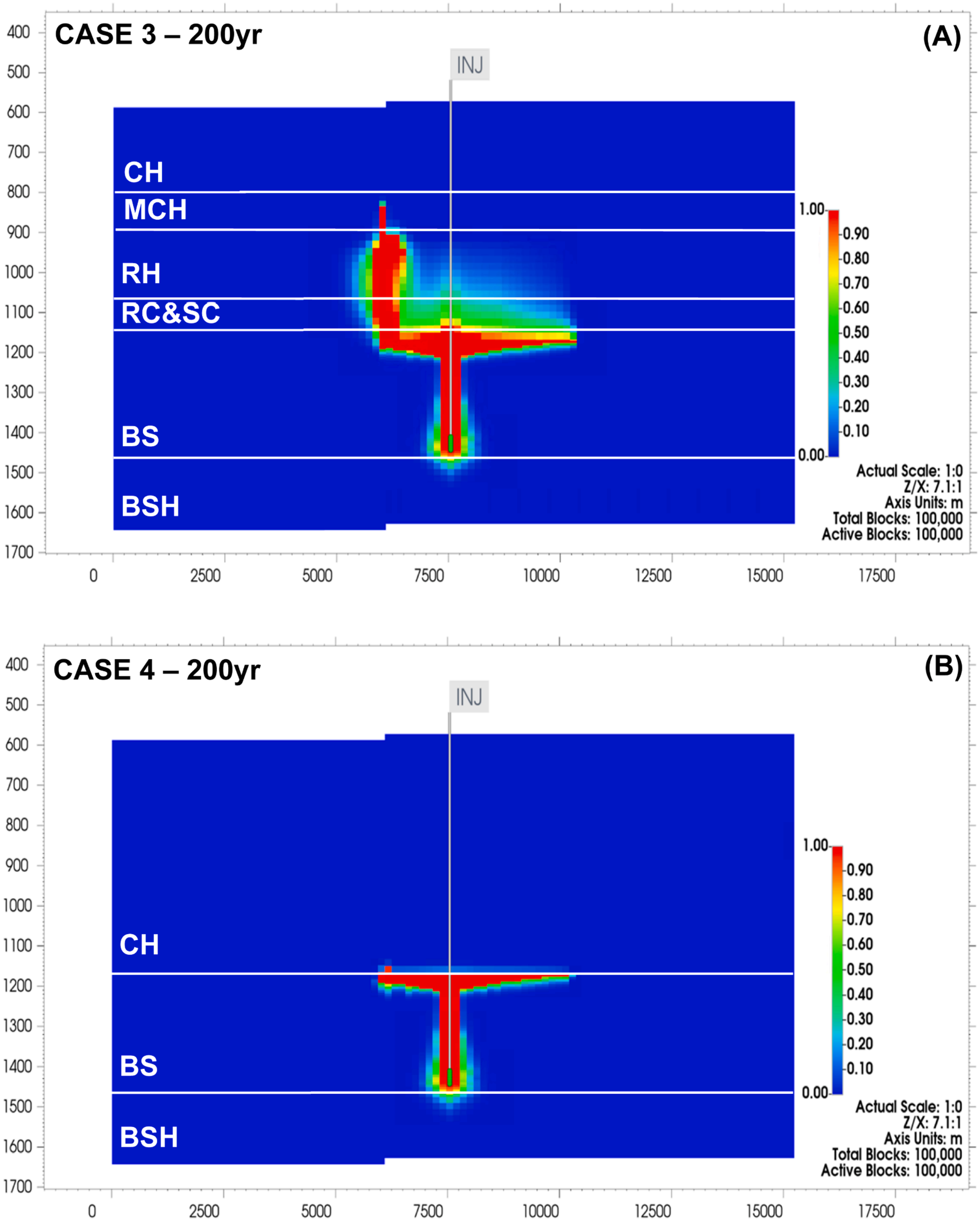

Fig. 19. Spatial distribution of the dissolved CO_2 mole fraction over the injection-period for Cases 3 and 4 (A&B) after 200 years simulation period, and for Cases 3 and 4 (C&D) after 1000 years of simulation period, respectively. The solid lines indicate the locations of boundaries of each lithology.

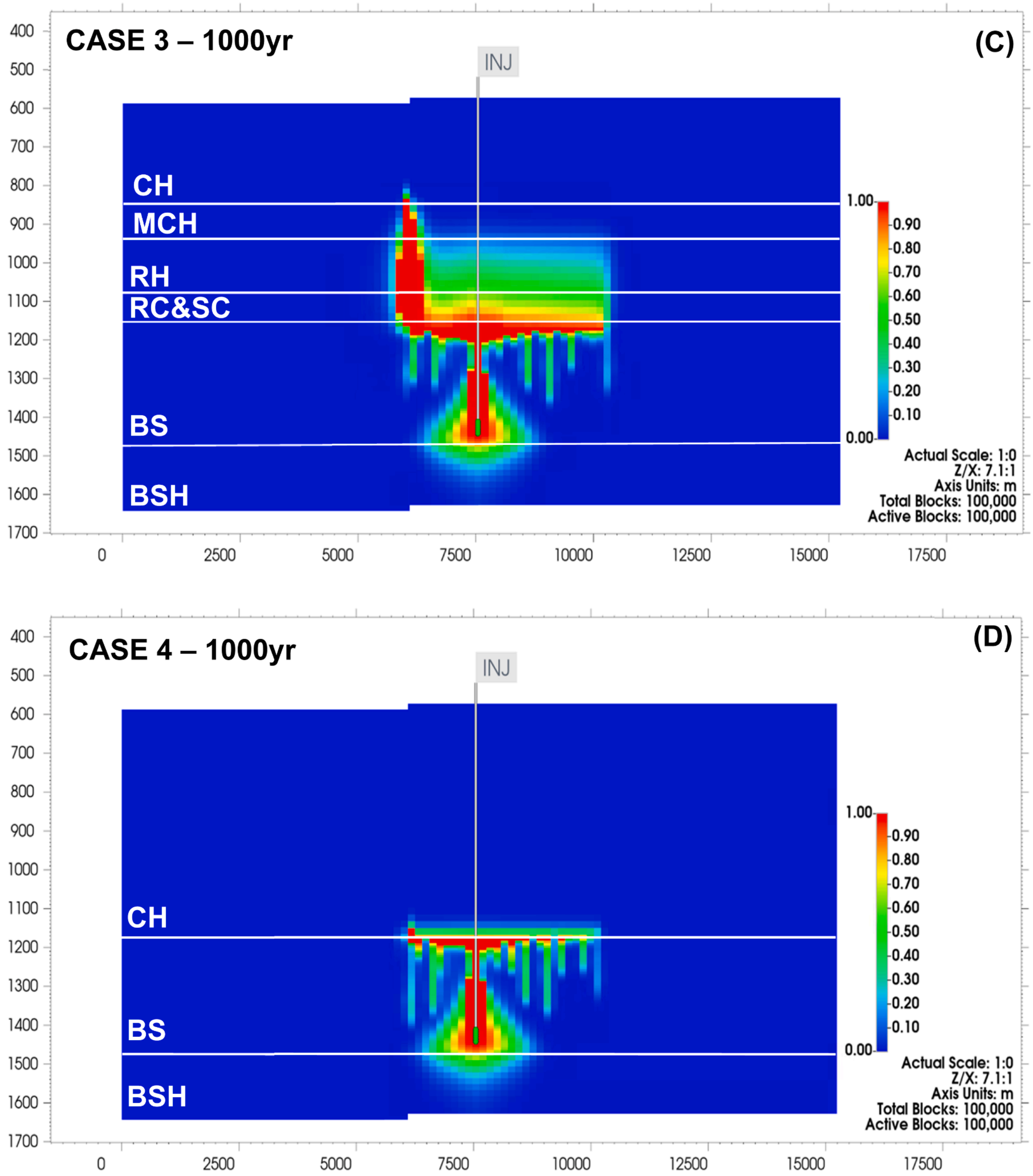

Fig. 19. (*continued*).

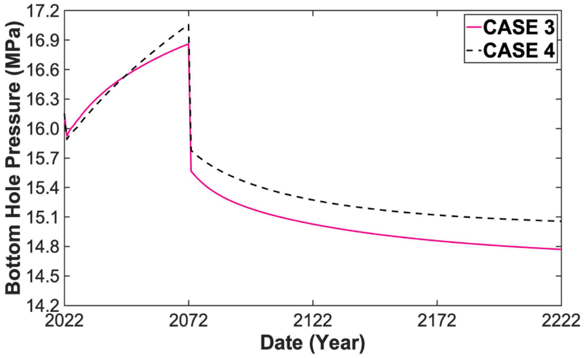

Fig. 20. The BHP profile over time for both Cases 3 and 4.

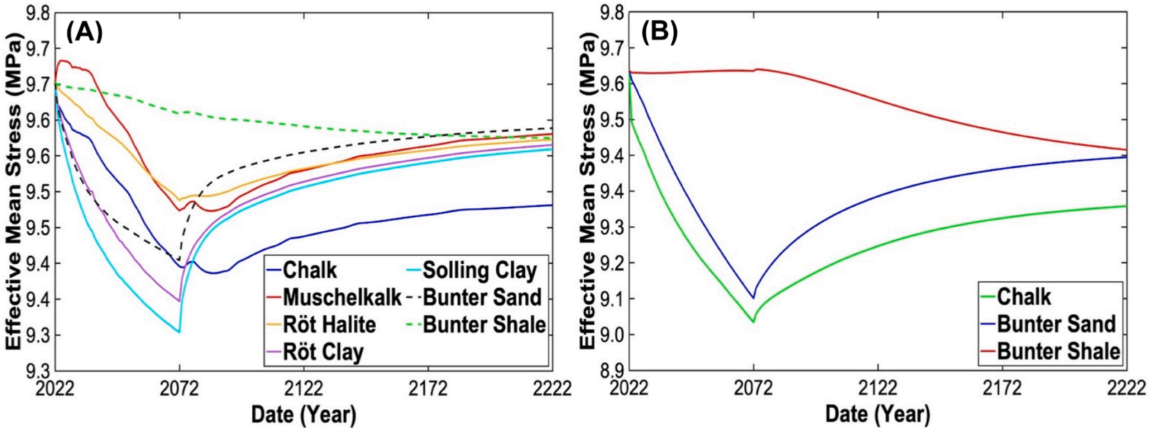

Fig. 21. Effective mean stress of each lithology within the model for Cases 3 and 4 after 200 years of simulation, with parts A and B corresponding to Cases 3 and 4, respectively.

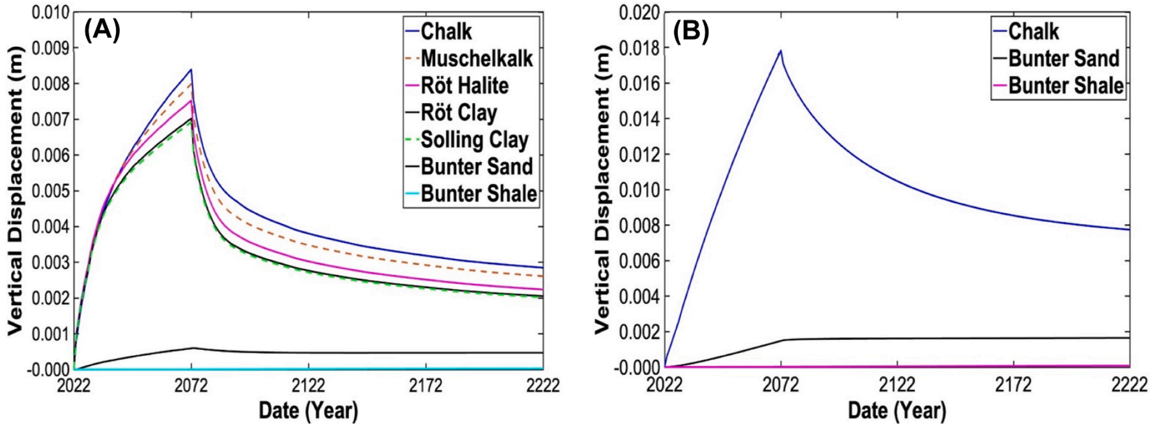

Fig. 22. Variation in volumetric expansion (ground uplift) of the reservoir and caprocks during the 200 years of simulation for Cases 3 (A) and 4 (B).

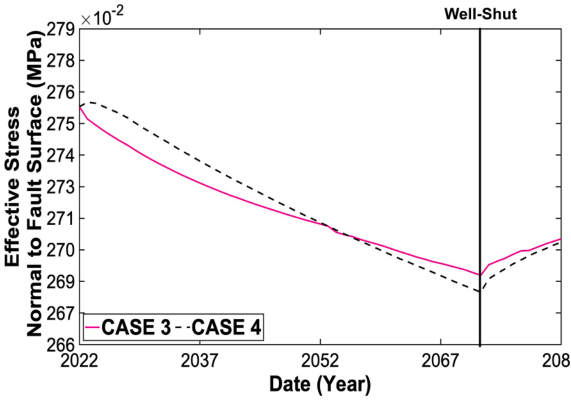

Fig. 23. Effective normal stress to fault surface change over time for both Cases 3 and 4. The black solid vertical line indicates the time of the end of injection.

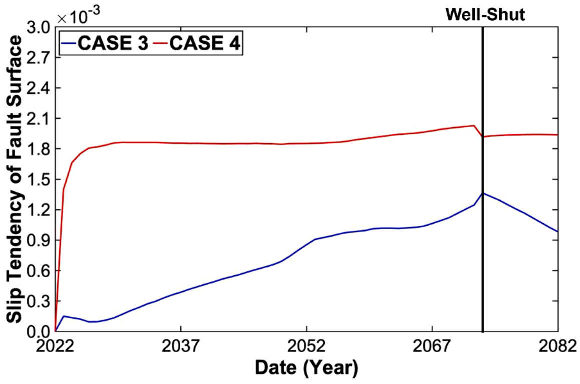

Fig. 24. Slip tendency (dimensionless) change as a function of time for both Cases 3 and 4. The black solid vertical line marks the end of the injection period.

Case 3, at the end of simulation was due to the dissolution of CO_2 and the larger precipitation of dolomite, feldspar, and quartz compared to Case 4. The spatial distribution of reduced pH extended, within the caprocks, vertically by 400 m (penetrating via the Solling Clay, Halite, and Muchelkalk, and ultimately, reaching the basement of the Chalk caprock sub-layer), and by 5945 m horizontally in Case 3, while in Case 4, it only expanded by 90 m in the vertical direction towards the Chalk caprock, and 5333 m in the horizontal direction as seen in Fig. 27**(A and B)**.

The significant difference in vertical expansion of the reduced pH region was influenced by the temporal variation of fault re-activation between the two Cases. The effects of different mineral compositions within the caprocks, between each of the Cases, was reflected in the varying degrees of buffering of pH. For example, at the end of the simulation period, the pH in the Solling Clay in Case 3 reduced to a value of 5.7, whereas for the Chalk in Case 4 it decreased to a value of 5.5. In addition, as not much gas front advancement is observed within the fault in Case 4, the pH within the caprock remained buffered at near-neutral

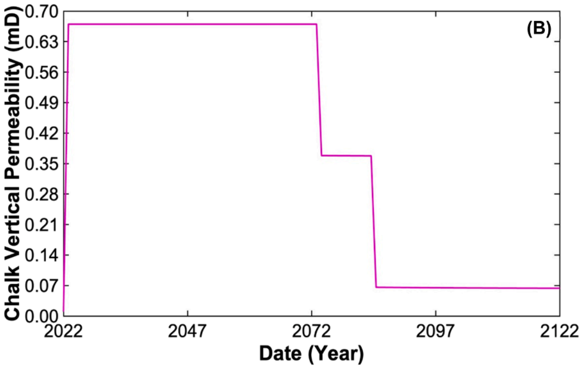

Fig. 25. Fault vertical permeability cutting through different caprocks for both Cases 3 (A) and 4 (B).

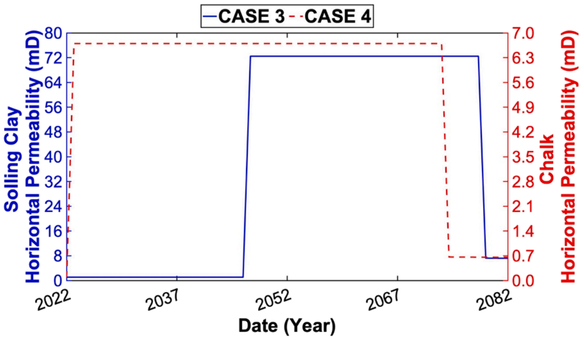

Fig. 26. Fault horizontal permeability cutting through different caprocks for both Cases 3 and 4.

values (between 7.09 to 6.8), as displayed in Fig. 27**(A and B)**.

The influence of the multi-layered caprock (Case 3) on the mineralogical changes was compared with that for the single caprock (Case 4). It can be observed that the $scCO_2$ plume penetrated to different degrees within the caprocks via the fault. Despite the slight change in the mineralogical composition of the caprock in response to $scCO_2$ injection, a noticeable difference was seen in calcite changes within the fault zone itself. During the 1000 years of simulation time, in Case 3, the Solling Clay, Chalk, and Muchelkalk caprock layers exhibited calcite dissolution, while the Röt Clay and Röt Halite faced calcite precipitation. In contrast, in Case 4, only calcite dissolution occurred as illustrated in Fig. 28**(A and B)**.

The porosity and calcite abundance values showed an inverse relationship throughout the caprock domain, suggesting that dissolution and precipitation mechanisms involving calcite predominantly control the changes in porosity. This is consistent with the intrinsically fast kinetics for calcite. Thus, the calcite had the largest change compared to the other minerals in both Cases during the 1000 years of simulation time. Therefore, calcite was the key mineral that caused the alteration of caprock porosity. Where the primary effect of gas advection is to increase CO_2 partial pressure and decrease pH values, it also makes calcite less thermodynamically stable in the caprock. Consequently, the interaction between Ca^{2+}, HCO_3^-, and pH regulates the dissolution and precipitation behaviour of calcite within the caprock domain. The different mineralogical changes had a direct influence on the caprock porosity change in both Cases 3 and 4. For instance, in Case 3, the Röt Halite caprock faced a decrease in porosity by 0.33 % due to the precipitation of calcite. whereas, in Case 4, the Chalk caprock porosity exhibited a rise by 0.1 % as displayed in Fig. 29**(A and B)**.

3. Trapping mechanisms of cases 1–4

Our series of simulations shows that, after a 1000-year simulation period, the majority of CO_2 remains in the supercritical phase. In order of relative occurrence, this is followed by CO_2 trapped due to the hysteresis effect, CO_2 in the dissolved phase, and finally, the smallest amount is trapped via mineralization as seen in Table 3. Further, the simulation results showed that the material balance errors for all Cases 1–4 were below 1 % after 1000 years of simulation period, and also the consistently low Newton cycles (2–4) indicate good numerical stability, proper model calibration, and efficient solver performance, whilst the occasional high peaks result from the tight convergence criteria used in the simulation as seen in Appendix Figs. A1 and A2.

Table 4 shows that the mole percentage of CO_2 leakage and the distance travelled from the reservoir into the caprocks were primarily influenced by the presence of chimneys and faults extending through the caprock layers. As a result, greater leakage volumes and longer migration distances were observed.

4. Conclusions

This paper presents a comprehensive simulation study that integrates flow, geomechanical, and geochemical processes within a 3D model using the CMG-GEM framework. A set of numerical simulations (Cases 1–4) was carried out to evaluate the integrity of both single and multi-layered caprocks in complex geological environments typical of potential CO_2 storage sites, such as those located in the North Sea. These geological heterogeneities included a complex sequence of shale and sand sub-layers, resembling a sandwich-like structure, with natural fractures within the thin shale sub-layers, along with geological faults. The key findings were:

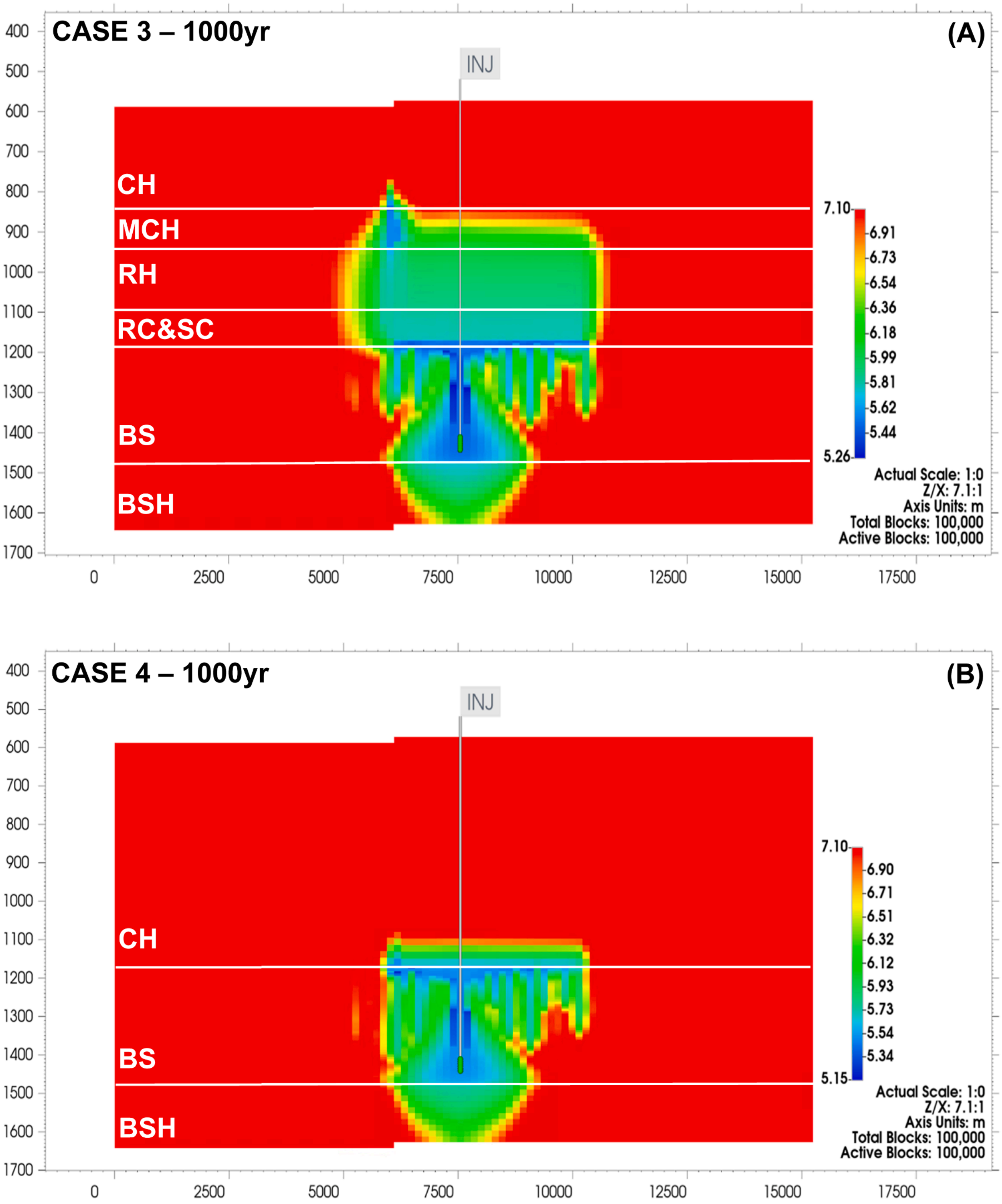

Fig. 27. The pH profile after 1000 years of simulation time for both Cases 3 (A) and 4 (B) is shown. The solid white lines indicate the boundaries of the lithologies in the model. The scale displays the pH values.

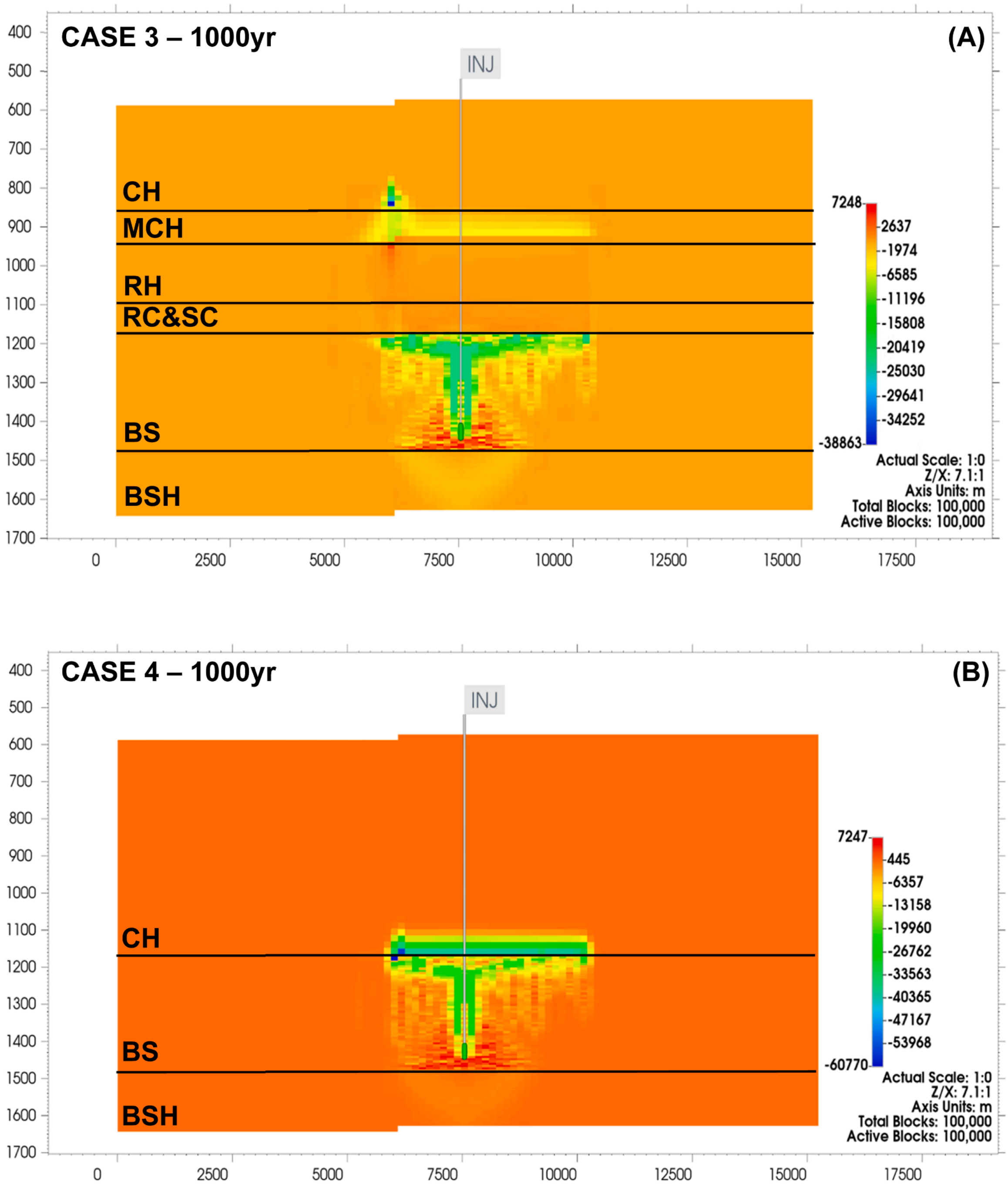

Fig. 28. IK plane view of calcite changes after 1000 years of simulation period for both Cases 3 (A) and 4 (B). The scale shows calcite change (kgmole).

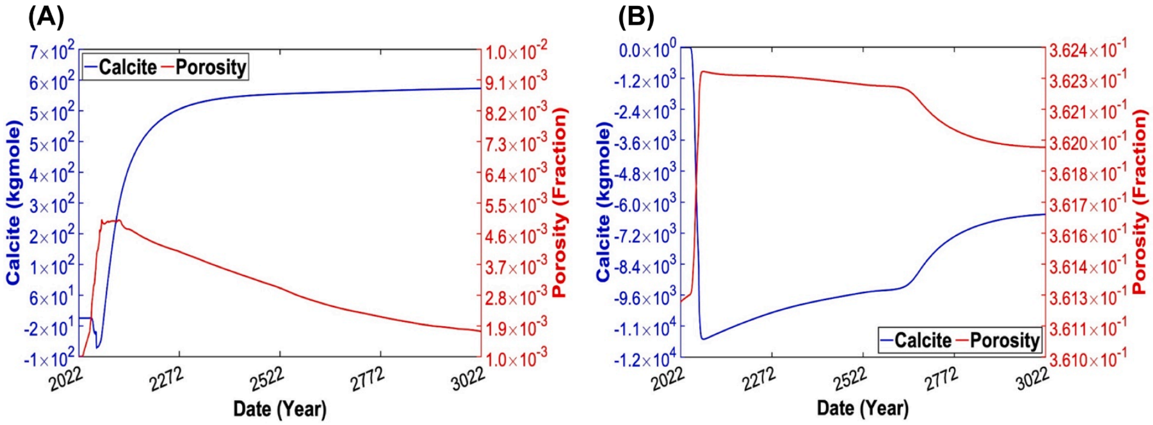

Fig. 29. Curves showing the variation in calcite (kgmole) and porosity change (fraction) over time of particular caprocks for both Cases 3 and 4, which were in Case 3, Röt Halite (A), and in Case 4, the Chalk (B). Positive values in the data indicate precipitation, whereas negative values indicate dissolution.

Table 3
Trapping mechanisms in each Case after 1000 years of simulation period for Cases 1–4. The prevalence of each mechanism is expressed as a percentage of total injected CO_2. The negative sign in mineral CO_2 trapping indicates a net release of CO_2 due to the dissolution of pre-existing carbonates. Over time, this process may stabilise, allowing more CO_2 to be permanently trapped as new carbonate minerals.

Trapping Mechanisms	%			
–	**CASE 1**	**CASE 2**	**CASE 3**	**CASE 4**
Supercritical	41	39	41	36
Trapped	38	37	35	32
Dissolved	23	26	27	35
Mineral	−2.6	−2.2	−2.7	−3.8
Total	100			

Table 4
Comparison of CO_2 leakage (in mole presentage) from the reservoir towards the caprock, including the extent to which the CO_2 plume migrated into the caprock in Cases 1–4 after 1000 years.

Cases	CO_2 Leakage Amount (in mole %)	Distance that CO_2 has already travelled into the caprock (m)
Case 1	60	350
Case 2	25	10
Case 3	80	355
Case 4	40	20

- The lateral movement of CO_2, once it reached the basement of the caprock, was primarily controlled by advection forces. These forces behaved differently in the single and multi-layered caprock systems. For example, in the multi-layered caprock system with fractured interlayers, the plume travelled laterally faster compared to single caprock system with fractured interlayers. This was due to the larger leakage of CO_2 from the reservoir towards the caprock via the chimney, where the plume travelled 350 m vertically, reaching the basement of the Chalk band after 50 years of continuous injection in the multi-layered caprock system with fractured interlayers.
- Calcite played a dominant role, overshadowing the effects of other mineral changes involving precipitation and dissolution. Consequently, calcite changes were crucial in controlling the caprock's porosity during the post-injection period, even within the short simulation period of 1000 years. Critically, mineral changes differed between the single and multi-layered caprock systems, as evidenced by the variations in halite and calcite behaviour in single and multi–layered caprock systems.
- The timing differences in fracture and fault reactivation caused a noticeable change in pressure in the Bunter Sandstone reservoir between cases. The reactivation of fractures and faults significantly affected the differing extents of caprock uplift in each of Cases 1–4.
- There was a noticeable difference in fault stability between the single and multi-layered caprock systems. This difference is evident in the late fault reactivation observed in the multi–layered caprock system compared to the single caprock system. Additionally, the vertical and horizontal permeability of the fault in the multi–layered caprock system showed a larger increase compared to that in the single caprock system, by 13 mD and 70 mD, respectively. This enhancement in permeability facilitated the upward migration of CO_2 through the fault pathway.
- Apart from the noticeable increase in caprock permeability resulting from the reactivation of fractures and faults, there were no significant changes in caprock porosity due to vertical displacement in the short-term simulation. Moreover, in the long-term simulation, mineral alterations were observed to have no substantial effect on caprock permeability in Cases 1–4.
- It was found that complex interactions and feedbacks, occurring between events and processes within the reservoir region and within the caprock, led to variant behaviours between the single and multi-layered caprock scenarios. This has demonstrated the need to include increased detail in both the geological model and the process simulations to properly capture the intricate effects observed here occurring during CO_2 injection and thereafter.

CRediT authorship contribution statement

Ali Alsayah: Writing – review & editing, Writing – original draft, Validation, Methodology, Investigation, Conceptualization. **Sean P. Rigby:** Writing – review & editing, Writing – original draft, Validation, Supervision, Resources, Project administration, Funding acquisition, Conceptualization.

Declaration of competing interest

The authors declare the following financial interests/personal relationships which may be considered as potential competing interests:

Sean P Rigby reports financial support was provided by University of Nottingham. Sean P Rigby reports a relationship with University of Nottingham that includes: employment. If there are other authors, they declare that they have no known competing financial interests or personal relationships that could have appeared to influence the work reported in this paper.

Supplementary materials

Supplementary material associated with this article can be found, in the online version, at doi:10.1016/j.ijggc.2025.104428.

Appendix A1

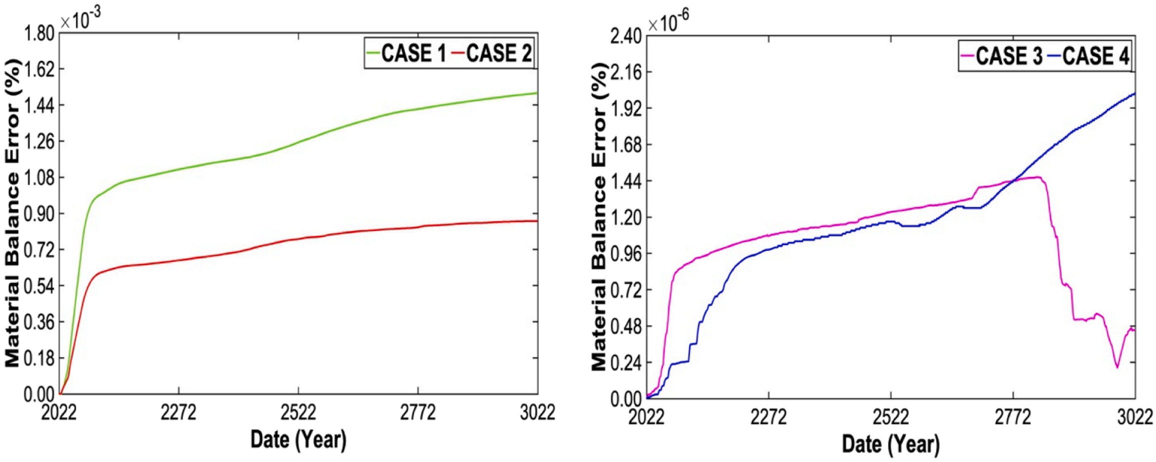

Fig. A1. Material balance error as a percentage during the 1000 years of simulation time for Cases 1–4.

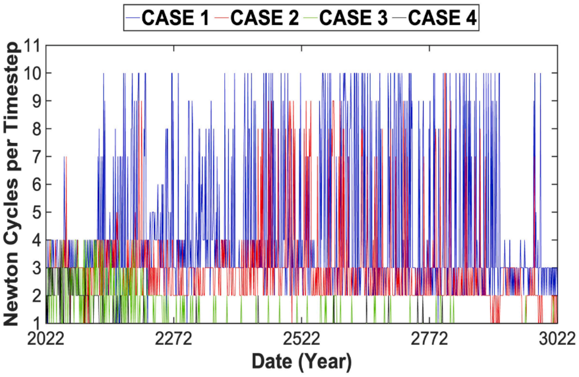

Fig. A2. Newton cycle per time during the 1000 years of simulation time for Cases 1–4.

Data availability

The data that has been used is confidential.

References

Agada, S., Kolster, C., Williams, G., Vosper, H., Macdowell, N., Krevor, S., 2017. Sensitivity analysis of the dynamic CO2 storage capacity estimate for the bunter sandstone of the UK Southern North Sea. Energy Procedia 114, 4564–4570.

Alsayah, A., Rigby, S.P., 2025. Impact of caprock complexity on carbon dioxide plume behaviour and storage security in the Bunter Sandstone Formation. Geo. Sci. Eng. 254, 214011.

Alshammari, A., Lakshmi, V., Brantley, D., Knapp, C.C., Knapp, J.H., 2022. Simulation of carbon dioxide mineralization and its effect on fault leakage rates in the South Georgia rift basin, southeastern US. Heliyon 8.

Aminu, M.D., Manovic, V., 2020. A modelling study to evaluate the effect of impure CO2 on reservoir performance in a sandstone saline aquifer. Heliyon 6, e04597.

André, L., Audigane, P., Azaroual, M., Menjoz, A., 2007. Numerical modeling of fluid–rock chemical interactions at the supercritical CO2–liquid interface during CO2 injection into a carbonate reservoir, the Dogger aquifer (Paris Basin, France). Energy Convers. Manag. 48, 1782–1797.

Bentham, M.S., Green, A., Gammer, D., 2013. The occurrence of faults in the Bunter sandstone formation of the UK sector of the Southern North Sea and the potential impact on storage capacity. Energy Procedia 37, 5101–5109.

Bentham, M., Williams, G., Vosper, H., Chadwick, A., Williams, J., Kirk, K., 2017. Using pressure recovery at a depleted gas field to understand saline aquifer connectivity. Energy Procedia 114, 2906–2920.

BP, 2021. Primary Store Geomechanical Model & Report: Key Knowledge Document. Department for Business, Energy & Industrial Strategy.

Cavanagh, A., Wildgust, N., 2011. Pressurization and brine displacement issues for deep saline formation CO2 storage. Energy Procedia 4, 4814–4821.

Clayton, C., Steinhagen, M., STEINHAGEN, H., Powrie, W., Terzaghi, K., Skempton, A., 1995. Terzaghi`s theory of consolidation, and the discovery of effective stress. (compiled from the Work of K. Terzaghi and AW Skempton). Proc. Inst. Civ. Eng.-Geotech. Eng. 113, 191–205.

DEPARTMENT OF BUSINESS & ENERGY AND INDUSTRIAL STRATEGY, 2022. North Sea Transit. Deal: One Year On 13.

ETI 2016. Bunter storage development Plan.

Figueiredo, B., Tsang, C.-F., Rutqvist, J., Bensabat, J., Niemi, A., 2015. Coupled hydro-mechanical processes and fault reactivation induced by CO2 injection in a three-layer storage formation. Int. J. Greenh. Gas Control 39, 432–448.

Gammer, D., Green, A., Holloway, S., Smith, G., 2011. The Energy Technologies Institute's UK CO2 storage appraisal Project (UKSAP). In: SPE Offshore Europe Oil and Gas Conference and Exhibition. SPE-148426-MS.

Gao, X., Yang, S., Shen, B., Tian, L., Li, S., Zhang, X., Wang, J., 2023. Influence of reservoir spatial heterogeneity on a multicoupling process of CO2 geological storage. Energy Fuels 37, 14991–15005.

Guo, B., Bandilla, K.W., Nordbotten, J.M., CELIA, M.A., Keilegavlen, E., Doster, F., 2016. A multiscale multilayer vertically integrated model with vertical dynamics for CO2 sequestration in layered geological formations. Water Resour Res 52, 6490–6505.

Heinemann, N., Wilkinson, M., Pickup, G.E., Haszeldine, R.S., 2012. CO2 storage in the offshore UK Bunter Sandstone Formation. Int. J. Greenh. Gas Control 6, 210–219.

Hollinsworth, A., De Jonge-Anderson, I., Underhill, J., Jamieson, R., 2024. Impact of reservoir quality on the carbon storage potential of the Bunter Sandstone Formation, Southern North Sea. Geoenergy 2 geoenergy2023-037.

James, A., Baines, S., Mccollough, S., 2016. Strategic UK CCS storage appraisal - initial screening and down-select. ETI.

Kano, Y., Funatsu, T., Nakao, S., Kusunose, K., ishido, T., LEI, X., Tosha, T., 2014. Analysis of changes in stress state and fault stability related to planned CO2 injection at the tomakomai offshore site. Energy Procedia 63, 2870–2878.

Khudaida, K.J., Das, D.B., 2020. A numerical analysis of the effects of supercritical CO2 injection on CO2 storage capacities of geological formations. Clean Technol. 2, 21.

Kivi, I.R., Makhnenko, R., Oldenburg, C., RUTQVIST, J., VILARRASA, V., 2022. Multi-layered systems for permanent geologic storage of CO2 at the gigatonne scale. Geophys. Res. Lett. 49, e2022GL100443.

Klimkowski, L., Nagy, S., Papiernik, B., Orlic, B., Kempka, T., 2015. Numerical simulations of enhanced gas recovery at the Załęcze gas field in Poland confirm high CO2 storage capacity and mechanical integrity. Oil Gas Sci. Technol. 70, 655–680.

Li, C., Hao, S., Zhang, S., Jiang, Y., Yi, Z., 2024. Simulation study on the mechanical effect of CO2 geological storage in Ordos demonstration area. *Water (Basel)* [Online] 16.

Liu, H., Hou, Z., Were, P., Gou, Y., Sun, X., 2014. Simulation of CO 2 plume movement in multilayered saline formations through multilayer injection technology in the Ordos Basin, China. Env. Earth Sci. 71, 4447–4462.

Liu, N., Pan, L., Cheng, J., 2017. Numerical modeling of CO2 and brine leakage through open fracture in a fault zone: open channel flow or Darcy flow. Geofluids 2017, 9035032.

Mazzoldi, A., Rinaldi, A.P., Borgia, A., Rutqvist, J., 2012. Induced seismicity within geological carbon sequestration projects: maximum earthquake magnitude and leakage potential from undetected faults. Int. J. Greenh. Gas Control 10, 434–442.

Morris, A., Ferrill, D.A., Henderson, D.B., 1996. Slip-tendency analysis and fault reactivation. Geology 24, 275–278.

Newell, P., Martinez, M.J., 2020. Numerical assessment of fault impact on caprock seals during CO2 sequestration. Int. J. Greenh. Gas Control 94, 102890.

Pekot, L., Ayash, S., Ge, J., Jiang, T., Jacobson, L., Gorecki, C., 2018. Results of CO2 storage efficiency in deep saline formations–Stage 2. 14th Greenh. Gas Control Technol. Conf. Melb. 21–26.

Pruess, K., Garcia, J., 2002. Multiphase flow dynamics during CO 2 disposal into saline aquifers. Environ. Geol. 42, 282–295.

Rinaldi, A.P., Jeanne, P., Rutqvist, J., Cappa, F., Guglielmi, Y., 2014a. Effects of fault-zone architecture on earthquake magnitude and gas leakage related to CO2 injection in a multi-layered sedimentary system. Greenh. Gases: Sci. Technol. 4, 99–120.

Rinaldi, A.P., Rutqvist, J., Cappa, F., 2014b. Geomechanical effects on CO2 leakage through fault zones during large-scale underground injection. Int. J. Greenh. Gas Control 20, 117–131.

Rinaldi, A.P., Vilarrasa, V., Rutqvist, J., Cappa, F., 2015. Fault reactivation during CO2 sequestration: effects of well orientation on seismicity and leakage. Greenh. Gases: Sci. Technol. 5, 645–656.

Romano, V., Bigi, S., Park, H., Valocchi, A.J., Hyman, J.D.H., Karra, S., Nole, M., Hammond, G., Proietti, G., Battaglia, M., 2023. A numerical model for gas CO2 migration in a fault zone. Pet. Geosci. 29 petgeo2022-092.

Sanchez, C. & Roehl, D. 2016. An equivalent continuum approach for the assessment of geological fault reactivation in hydrocarbon reservoirs.

Tillero, E., Mogollon, J.L., Tillero, F., 2024. De-risking Saline Aquifer-type CO2 storage resources via machine learning-based reservoir modelling. Case Study. Bunter Sandstone Formation, Southern North Sea.

Vilarrasa, V., Bolster, D., Olivella, S., Carrera, J., 2010. Coupled hydromechanical modeling of CO2 sequestration in deep saline aquifers. Int. J. Greenh. Gas Control 4, 910–919.

Watson, F.E., Mathias, S.A., Daniels, S.E., JONES, R.R., Davies, R.J., Hedley, B.J., Hunen, J.V., 2014. Dynamic modelling of a UK North Sea saline formation for CO_2sequestration. Pet. Geosci. 20, 169–185.

Williams, J.D.O., Holloway, S., Williams, G.A., 2014. Pressure constraints on the CO_2storage capacity of the saline water-bearing parts of the Bunter Sandstone Formation in the UK Southern North Sea. Pet. Geosci. 20, 155–167.

Williams, J.D.O., JIN, M., Bentham, M., Pickup, G.E., Hannis, S.D., Mackay, E.J., 2013. Modelling carbon dioxide storage within closed structures in the UK Bunter Sandstone Formation. Int. J. Greenh. Gas Control 18, 38–50.

Xiao, T., Xu, H., Moodie, N., Esser, R., Jia, W., Zheng, L., Rutqvist, J., Mcpherson, B., 2020. Chemical-mechanical impacts of CO2 intrusion into heterogeneous caprock. Water Resour. Res. 56.

Zhang, D., Fan, C., Kuang, D., 2019. Impact assessment of interlayers on geological storage of carbon dioxide in Songliao Basin. Oil Gas Sci. Technol.–Rev. IFP Energ. Nouv. 74, 85.

Zhong, Y., Li, Q., Xu, L., Wen, Y., Hou, Y., Gao, W., 2024. Two-phase flow behavior in CO2 geological storage considering spatial parameter heterogeneity. Greenh. Gases: Sci. Technol. 14, 11–25.

Zulqarnain, M., Zeidouni, M., Hughes, R.G., 2020. Hydromechanical modelling to evaluate impact of fault structure on CO2 migration in stacked storage system. Int. J. Greenh. Gas Control 93, 102886.